Boltzmann sampling of frustrated J_1-J_2 Ising models with programmable quantum annealers

Elijah Pelofske [*]

Information Systems & Modeling, Los Alamos National Laboratory, Los Alamos, New Mexico 87545, USA;
Theoretical Division, Quantum & Condensed Matter Physics, Los Alamos National Laboratory, Los Alamos, New Mexico 87545, USA;
and Center for Quantum Computing, Los Alamos National Laboratory, Los Alamos, New Mexico 87545, USA

(Received 5 November 2025; accepted 13 August 2026; published 8 September 2026)

One of the surprising, and potentially very useful, capabilities of analog quantum computers, such as D-Wave quantum annealers, is sampling from the Boltzmann, or Gibbs, distribution defined by a classical Hamiltonian. In this study, we thoroughly examine the ability of D-Wave quantum annealers to sample from the Boltzmann distribution defined by a canonical type of competing magnetic frustration J_1-J_2 model, the one-dimensional ANNNI (axial next-nearest-neighbor Ising) model. Boltzmann sampling error rate is quantified for standard linear-ramp anneals ranging from 5 ns annealing times up to 2000 µs on two different D-Wave quantum annealing processors. Interestingly, we find some analog hardware parameters that result in a very high accuracy (down to a total variation distance of 0.0003) and low-temperature sampling (down to $\beta = 32.2$) in a frustrated region of the ANNNI model magnetic phase diagram. This bolsters the viability of current analog quantum computers for thermodynamic sampling applications of highly frustrated magnetic spin systems.

DOI: 10.1103/2xc3-815x

I. INTRODUCTION

The ANNNI (axial next-nearest-neighbor Ising) model was first introduced as a model for the complex magnetic ordering of certain rare-earth compounds [1,2], and subsequently has been extensively studied because it exhibits a variety of rich magnetic phenomena, including various phase transitions, Devil's staircase of commensurate and incommensurate phases, and in general providing a simple-to-define Ising model with controllable frustration [3,4]. The ANNNI model is the prototypical J_1-J_2 frustrated magnetic model. The general class of interactions characterized by short-range particle attraction and long-range particle repulsion yields a rich class of phenomenology [5], and the one-dimensional (1D) ANNNI model is arguably the simplest version of this type of interaction. These types of frustrated competing interaction models have been subsequently generalized not only to higher dimensions, but also to include both thermal and quantum fluctuations to drive state transitions and time dynamics of these models [3,6–10]. Here, we will consider the original, classical, Ising model form of the 1D ANNNI model, given by

$$\mathcal{H}_{\mathrm{ANNNI}} = -J_1 \sum_i S_j S_{i+1} + J_2 \sum_i S_i S_{i+2},$$

where $-J_1 > 0$ is the nearest-neighbor ferromagnetic coupling and $J_2 > 0$ is the antiferromagnetic coupling on the next-nearest neighbors, and S_i are the spins that in this case will be simulated by qubits. No local fields, h_i, are present in this model.

This study addresses how well current analog quantum computers, specifically D-Wave quantum annealers, can sample from the Boltzmann distribution defined by classical ANNNI models at various points in the frustrated magnetic phase diagram. Quantum annealing is a quantum computational algorithm that aims to find good solutions of combinatorial optimization problems using the principles of quantum adiabatic evolution [11–15]. Noisy quantum annealers have been physically created, and one of the surprising findings is that they are quite effective at being programmable magnetic system simulators [16–22], and moreover can, surprisingly, be efficient Boltzmann (thermal) samplers of classical, and potentially even quantum, Hamiltonians [23–34]. The core computational capability that is of interest is being able to efficiently approximate the Boltzmann distribution defined by a classical Ising model;

$$p(z) \propto e^{-\beta H(z)}, \tag{1}$$

where $p(z)$ is the probability distribution over z spin configurations. $H(z)$ is the classical Hamiltonian evaluation of the energy of a particular configuration. β is the inverse thermodynamic temperature $\beta = 1/k_B T$, and we use natural units of the Boltzmann constant $k_B = 1$ for numerical computations and visual plots. Note that we will generally refer to this sampling task as Boltzmann sampling; however, this can be equivalently referred to as either Gibbs sampling or thermal sampling. Boltzmann sampling, equivalently Gibbs sampling, is an important computational capability for many domains in information processing [35–40], and finding novel ways of speeding up this computation is an active area of study [41–44].

[*]Contact author: epelofske@lanl.gov

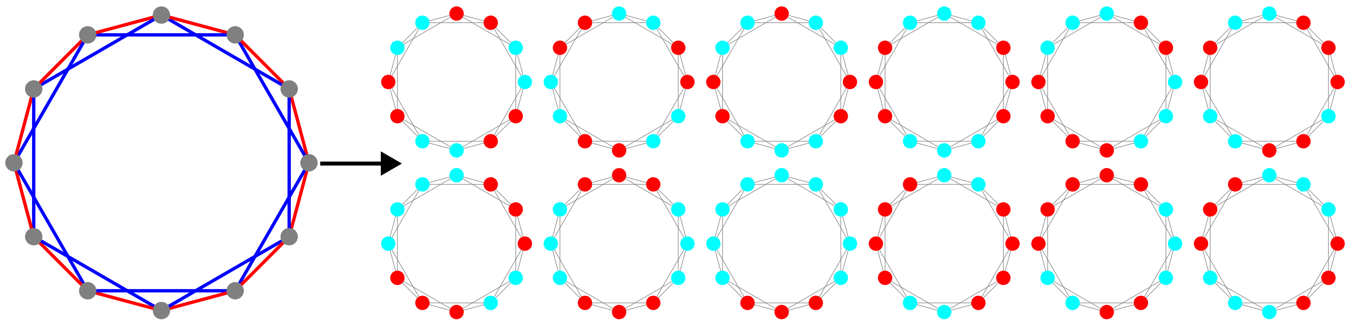

FIG. 1. Twelve-spin ANNNI model rendering (left), where red edges represent ferromagnetic coupling and blue edges represent antiferromagnetic coupling. This model is then sampled on the D-Wave QPU hardware; representative sampled spin configurations are shown on the right. Cyan nodes are spin-down ↓ and red nodes are spin-up ↑. These samples are from 5 ns annealing times, with frustration parameter coupling of $J_2 = 0.5$ (bottom row) and $J_2 = 1$ (top row). All of these spin configurations were measured on `Advantage2_prototype1.4`.

The overall open question is how well the analog quantum hardware performs as a Boltzmann sampler of the ANNNI model in the different regions of the magnetic phase diagram. For example, it could be reasonable to assume that near or at the maximum frustration point, the analog hardware struggles with unbiased sampling, and therefore perhaps would be a worse Boltzmann sampler in that regime. However, maybe that is not the case; we need to test it to see what the results are—and if the analog hardware is a good Boltzmann sampler in very highly frustrated regimes, which could be interesting because those regimes are also where more sophisticated classical Monte Carlo update schemes are needed.

The ANNNI model has recently been studied in the context of sampling-based quantum algorithms, including quantum annealing. For example, Ref. [45] numerically studied quantum annealing simulation of the 1D ANNNI model using infinite time evolving block decimation. Reference [46] used a digital nonvariational feedback-based quantum algorithm to study properties of the 1D quantum ANNNI model. Reference [47] studied the 1D quantum ANNNI model using a variety of techniques, including tensor network approximations and quantum neural networks. Reference [48] studied equilibrium simulations of the two-dimensional (2D) classical J_1-J_2 (ANNNI) model using D-Wave quantum annealers.

II. METHODS

The specific type of analog quantum computers we use in this study is superconducting flux qubit quantum annealers that operate at approximately 15 mK, manufactured by the commercial company D-Wave [49–53]. The physical Hamiltonian that the analog D-Wave processors implement is

$$\mathcal{H} = -\frac{A(s)}{2}\left(\sum_i \sigma_x^{(i)}\right) + \frac{B(s)}{2}\left(\sum_i h_i\sigma_z^{(i)} + \sum_{i>j} J_{i,j}\sigma_z^{(i)}\sigma_z^{(j)}\right),$$

where $A(s)$ defines the transverse field strength over time, controlled by the normalized parameter $s \in [0, 1]$, and $B(s)$ similarly controls the energy scale of the classical Hamiltonian that we wish to sample. h_i and $J_{i,j}$ are the user-programmable coefficients that define the Ising model we want to sample configurations of. The transverse field term $\sum_i \sigma_x^{(i)}$ does not commute with the diagonal Z basis terms, and thereby is the driving mechanism in the quantum annealing processor that facilitates state transitions. At the end of each anneal, the state of each (active) qubit is measured in the computational (Pauli-Z) basis.

Only two hardware control parameters are adjusted for these Boltzmann distribution sampling simulations. The first is the total annealing time, ranging from 2000 μs to 5 ns. The second is the analog coupler energy scale, which we artificially set to values weaker than the maximum that the hardware allows by turning off `auto-scale`. The tuning of both of these parameters is motivated by prior studies that have shown that both of these mechanisms change the quality and the effective temperature of the Ising model sampling [26–28]. In particular, degeneracy lifting due to the transverse field for particular Ising models can cause thermodynamic sampling issues where configurations within the same energy level, in particular, the ground-state energy, can be nonuniformly sampled [54–62]. In general, it has been shown that these issues can be mitigated by reducing the programmed energy scale of the Ising model on the analog hardware [26–28]. All other D-Wave QPU settings are left to default values; in particular, only the standard linear-ramp anneals are used.

The specific model we use is a 12-spin ANNNI model, with periodic boundary conditions. The periodic boundary conditions remove edge effects and allow us to approximate the thermodynamic limit better than with open boundaries. The relatively small system size makes the numeric computations for fitting the thermodynamic sampling properties more tractable compared to larger spin systems, where some approximations of the true Boltzmann distribution would likely be required. Figure 1 shows a rendering of the ANNNI model, along with some representative spin configurations measured on the D-Wave QPUs. The phase diagram of the ANNNI model has been extensively studied [3,63–70], but for the purposes of this study, the goal is to approximately sample from the Boltzmann distribution defined by the classical 1D ANNNI model at various frustration parameters defined by the next-nearest-neighbor antiferromagnetic coupling J_2. $J_2 < 0.5$ is the ferromagnetic portion of the phase diagram, where the spins tend to be aligned. $J_2 = 0.5$ is a critical frustration point (also known as a multiphase point) and denotes the

TABLE I. Summary of the D-Wave QPUs used in this study, including the number of independent disjoint native embeddings of the ANNNI model used for each processor graph.

D-Wave QPU chip	Graph name	Qubits	Couplers	Disjoint native embedding count
`Advantage_system4.1`	Pegasus P_{16}	5627	40 279	337
`Advantage2_system1.4`	Zephyr Z_{12}	4593	41 796	204

boundary between the ferromagnetic phase and the antiferromagnetic phase. At $J_2 > 0.5$, the spin ordering becomes antiferromagnetic, with various terms being used for the particular spin grouping, ranging from superantiferromagnetic, antiphase, and even stripe phase in the case of 2D ANNNI. Concretely, the $J_2 > 0.5$ ground-state spin pattern is $\uparrow\uparrow\downarrow\downarrow\uparrow\uparrow\cdots$, which we can see some examples of in the spin configurations shown in Fig. 1. These main ordered phases are specifically for the low-temperature regions of the phase diagram; at high temperatures, the model becomes more disordered. One of the primary questions that the ANNNI model lets us investigate with regard to quantum annealer sampling capabilities is to evaluate whether there is a significant difference within regions of high frustration, and at the critical frustration point of $J_2 = 0.5$ as well as just before and after the critical frustration point. Therefore, we sample the ANNNI model at the frustration parameters of $J_2 = 0.01, 0.25, 0.49, 0.5, 0.51, 0.75, 1.0$. Classical Monte Carlo sampling methods are extremely efficient for this model because the system size is small. This system size is ideal for extensive physical analog hardware parameter study, where ground truth is efficient to compute. Future studies should examine sampling properties at larger system sizes with analog quantum computing hardware in comparison to classical methods.

We use a direct spin-to-qubit mapping of the Ising model onto the QPU hardware graph. This is accomplished specifically using the Glasgow subgraph isomorphism finder [71], part of the `minorminer` package [72,73]. This isomorphism finder is applied iteratively to the hardware graphs in order to find many disjoint embeddings of the Ising model onto the QPU graph. This then enables many independent configurations of the Ising model to be sampled within the same anneal-readout cycle, in parallel [60,74,75]. Table I details the D-Wave QPU hardware graph specifications, along with how many of these parallel embeddings are used. The QPU hardware graphs are called Pegasus [76,77] and Zephyr [78], which have slightly different connectivities. One of the primary advantages of using a direct spin-to-qubit mapping on the hardware, as opposed to using minor embeddings, is that we remove various thermodynamic sampling issues, not to mention additional sources of error, caused by minor embedding [79]. No other types of error mitigation, besides independently embedded instances within the same anneal-readout cycle, were used (no readout bias mitigation, and no gauge transforms were applied). Appendix B shows the exact embeddings on the hardware graphs.

The total number of samples obtained for each hardware parameter combination of annealing time, energy scale, ANNNI frustration parameter (J_2), and D-Wave device is exactly 1000 anneal-readout cycles, multiplied by the disjoint embedding count shown in Table I (337 000 samples on `Advantage_system4.1` and 204 000 samples on `Advantage2_system1.4`). This means that the results from the `Advantage_system4.1` device had a larger total sample count, which could make the results for that device better than the other QPU. For annealing times greater than 100 μs, the maximum QPU time limit of the D-Wave software prevents jobs with a full 1000 anneals, and therefore for the longer annealing times four device jobs are used, each using 250 anneals.

The experimental settings we apply are as follows. The energy scales that are evaluated are in the range 0.01–1.0 in steps of 0.01, along with 0.0001, 0.0005, 0.001, 0.005. These energy scales are in normalized hardware programmable units, with more details given in Appendix A. These energy scale normalizations are applied to the entire ANNNI model. This means that the magnetic interactions in the ANNNI model are the same relative to each other, but on the analog quantum hardware the corresponding sampling properties are different, due to a variety of mechanisms. To this end, when reporting results we will report both the overall J energy scale, between 0 and 1, as well as the ANNNI model frustration parameter J_2. The annealing times used are 5 through 100 ns, in steps of 1 ns, then 200, 300, 400, 500, 600, 700, 800, and 900 ns, then 1 through 100 μs in steps of 1 μs, and then 200 through 2000 μs in steps of 100 μs. The reason for these analog parameter ranges is to cover a reasonably fine resolution search from the minimum to the maximum possible values (where the minimum coupling energy scale is simply a sufficiently small value close to the precision limit of the hardware).

There is evidence from Kibble-Zurek mechanism [80,81] scaling that the dynamics of the QPU in the very fast annealing times [82] are closed-quantum system coherent dynamics [83–85]. Then, at much longer annealing times, the system becomes a quasistatic open quantum system [29,86]. In general, these processors have a variety of sources of error and noise contributing to the observed dynamics, including spurious qubit coupling, spin bath polarization, and noise drift over time [25,27,87–91]. All of these sources of error can be nonideal for Boltzmann sampling, for instance, spin bath polarization causes anneal-readout sequences measured near to each other in time (e.g., a single device "job") to be correlated.

Note that during the execution of these experiments, there were hardware changes of the `Advantage2_prototype1.4` graph, where several qubits and edges were unexpectedly deactivated; this affected some of the disjoint minor embeddings, which were discarded in the postprocessing stage. The disjoint embedding count of 204 accurately reflects the data reported in this study, and the qubit and coupler counts are for the more current hardware, and for consistency the chip Id of `Advantage2_prototype1.4` is used throughout the text.

Next, we need an error rate measure between two probability distributions in order to quantify how well the quantum annealing hardware approximates a Gibbs distribution at a particular temperature. To this end, we use total variation distance (TVD), defined for two probability distributions $P(x)$ and $Q(x)$ as

$$\mathrm{TVD} = 0.5 \sum_x |P(x) - Q(x)|. \tag{2}$$

This error rate measure is minimized when it is 0, meaning the two distributions are identical, and if the TVD is 1 then the distributions are entirely disjoint. Typically, the maximum possible error rate we will see is 0.5, which corresponds to the approximate distribution being disordered with respect to the correct distribution. The full Boltzmann distribution fitting process is performed using a combination of black-box optimization solvers in scipy [92] and a rigorous gridsearch. The fitting is performed independently for each analog hardware parameter range. Because of the finite sampling effect, in many cases the best fitted distribution has many different values of β that result in the same error rate—In this case, in plots, we report the error bar of the full β range if the range exceeds 0.1. And when reporting single β values in the case where the β error surface is flat, we report the average β value that gives that minimum TVD error measure. The following black-box optimizers were used, each being independently initialized at 28 different values of β ranging from 10^5 to 10^{-8}; `nelder-mead` [93], `cobyla`, `l-bfgs-b`, `powell`, `slsqp` [94], `trust-constr` [95], and `tnc`. The grid search is then performed over 100 β values in logarithmically spaced intervals from 10^{-3} to 10^{-15}. An additional gridsearch over β starting at 10^{-4} in steps of 10^{-4} is performed until sufficiently large β values result in division by zero errors. All TVD values and β values are rounded to reasonable numerical precision of at least seven decimal places. At the end of the process, the relevant quantity we extract is simply what the absolute minimum TVD that was found, and then what the corresponding β is of that distribution. The computation of the thermal distribution fitting was greatly accelerated by the Python 3 libraries Numba and Numpy [96,97]. Appendix C shows some examples of this temperature fitting procedure, including instances of flat response surfaces where different β values result in the same TVD. The temperature fitting process is independently performed for the distribution (each distribution consisting of either 337 000 or 204 000 ANNNI model measurements) defined by each unique hardware parameter combination defined by the four tuple of D-Wave QPU, annealing time, overall J energy scale, and J_2 frustration parameter.

III. RESULTS

Figure 1 details some representative spin configurations sampled on one of the D-Wave QPUs, showing some of the differences in the magnetic ordering seen when the frustration parameter of the ANNNI model changes.

The experimental question is, given we are able to tune the analog hardware control properties of the coupler energy scale and the total annealing time, what is the absolute lowest error rate Boltzmann sampling that can be achieved?

To this end, Figs. 2 and 3 plot β corresponding to the minimum error rate found across all evaluated annealing times, as a function of the J energy scale. The seven different lines show the results for different ANNNI model frustration parameters, ranging from $J_2 = 0.01$ (ferromagnetic ordering region of the model phase diagram) to $J_2 = 1.0$ (the more frustrated region). These plots show what the absolute lowest fitted error rate is for each version of the ANNNI model at different frustration parameters, and then what the corresponding sampling temperature is in the top subplots. Notably, the model with the lowest error rate overall, on both QPUs, is unexpectedly the highly frustrated $J_2 = 1 = J_1$. Table II lists the absolute lowest error rates and what the corresponding physical analog parameters were that produced that distribution. Appendix D analyzes sample convergence for some representative D-Wave device distributions, showing that the lowest reported error rates are stable. The newer of the two processors, `Advantage2_system1.4`, which has a Zephyr connectivity graph, is able to achieve lower error rates compared to the `Advantage_system4.1` processor, at some value of β, for all ANNNI frustration parameters except $J_2 = 0.49$. Note that the y axis scales in Figs. 2 and 3 for β (top subplots) were cut off at very small β for improved visual interpretability, those points corresponding to very weak hardware J coupling, and therefore close to random sampling and therefore very high-temperature sampling. Interestingly, we see that in general the highest error rates are seen for the critical frustration point at $J_2 = 0.5$ or the models with frustration near the critical point with $J_2 = 0.49, 0.51$.

Figures 4 and 5 provide more detail on the sampling characteristics over different annealing times, in the form of scatterplots between the best-fitted TVD versus β, where each point on the subplots is a different annealing time. These show that the sample distribution changes dramatically as both annealing time and the entire J energy scale are changed. Figures 4 and 5 show specifically simulations from the ANNNI model at the critical frustration point, and the general quality of these simulations is that the TVD error rate is quite high. Notably, these plots show that the estimated β spans a wide range of possible values (mostly at higher temperatures)—overall showing that for most of these energy scales (except at very small values, less than ≈ 0.2), there is significant uncertainty of the effective temperature of the sampled distributions. This holds true for a majority of annealing times on the `Advantage2_system1.4` processor, and these estimated temperature ranges when the overall energy scale is greater than ≈ 0.5 typically span more than an order of magnitude. In the temperature fitting process, what this corresponds to is that there is a wide range of inverse temperatures that all result in the same TVD, up to numerical precision. This result is a fairly unique characteristic of sampling at this high-degeneracy critical frustration point at $J_2 = 0.5$—looking at slightly different J_2 frustration parameters, such as Figs. 6 and 7, there is not this prevalence of temperature distribution fitting uncertainty. This suggests that this specific inverse temperature fitting uncertainty resulting from high-energy-scale quantum annealer sampling is a sensitive probe of critical frustration points of spin models and could be especially prominent because of finite sampling. For context, the degeneracy at $J_2 = 0.5$ is $(\frac{1+\sqrt{5}}{2})^{12} \approx 322$ (the golden ratio to the power of N) [3,98].

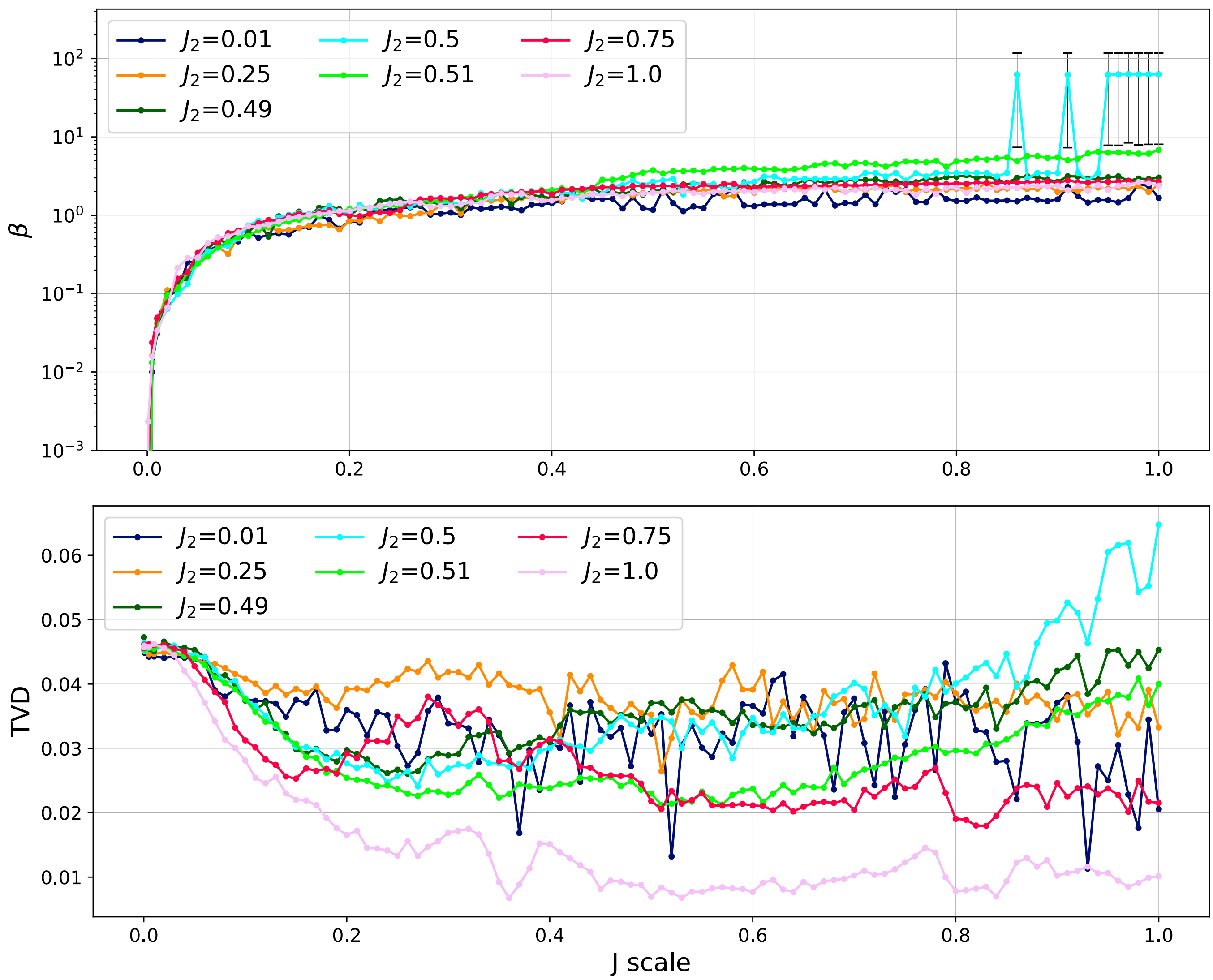

FIG. 2. Minimum error rate (TVD), from all evaluated annealing times, Boltzmann sampling as a function of the J coupling energy scale programmed on the analog hardware (x axis), for the `Advantage_system4.1` D-Wave quantum annealing processor. The bottom plot shows the value of the minimum error rate, TVD, found across all evaluated annealing times, and the top plot shows the corresponding β value at which the QPU samples a Boltzmann distribution at that given error rate. Each separate line denotes a different ANNNI model frustration parameter J_2.

Next, Fig. 6 directly compares ANNNI frustration parameters slightly into the ferromagnetic phase ($J_2 = 0.49$) and slightly into the antiphase (antiferromagneticlike) region ($J_2 = 0.51$), at different analog hardware energy scales run on the Zephyr graph QPU. Figure 7 does the same, but on the Pegasus graph QPU. The primary notable observation is that these two different ANNNI models do exhibit dramatically different characteristics. This suggests that, as approximate Boltzmann samplers, analog quantum annealers are sensitive to frustrated models at different regions in a magnetic phase diagram—in particular, separated by a critical frustration point. Generally, when the energy scale on the hardware is larger, the error rates become much larger for faster annealing times and lower for longer annealing times.

Because the very fast anneals used here, e.g., down to 5 ns, are within the coherence time of the processor, these computations are coherent quantum quenches. It is therefore interesting to note that some of the very fast quenches produce distributions that approximate a Boltzmann distribution of the classical ANNNI model reasonably well—See, for example, the low-energy scale plots in Fig. 7 for the frustration parameter of $J_2 = 0.49$. The important caveat to this observation is that at the full energy scale of the J couplers, the distributions that are produced are very much not thermal—In order for these fast anneals to approximately sample thermal distributions, the coupling energy scale must be reduced. Because of the quench dynamics of these fast anneals, it is plausible that the distributions that are produced happen to be close to relatively high-temperature distributions. Importantly, the D-Wave quantum annealers cannot measure in the X basis or any basis except the computational Z basis. Therefore, we are not able to examine what sorts of dynamics are occurring here to lead to relatively low-error-rate approximations

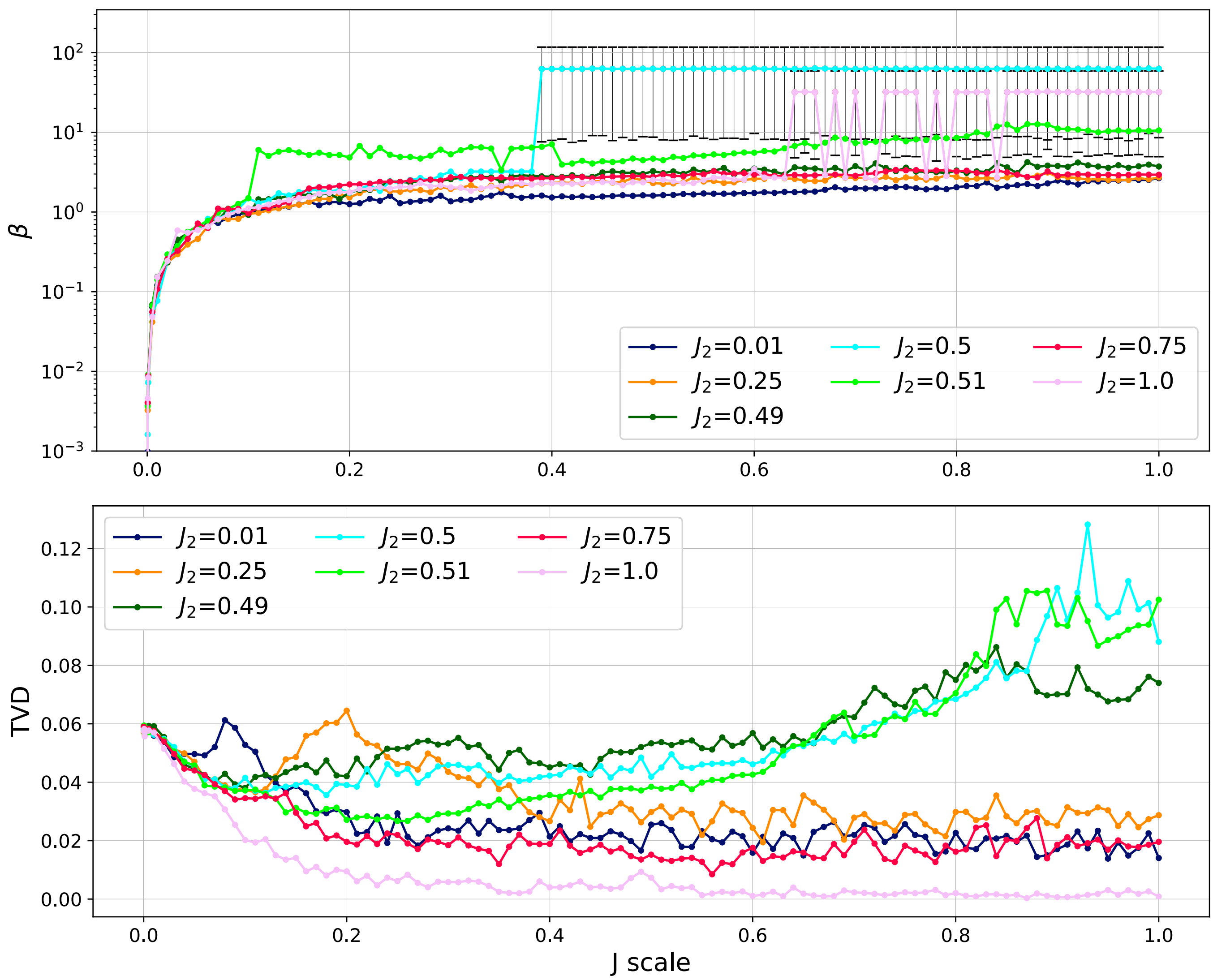

FIG. 3. Minimum error rate (TVD), from all evaluated annealing times, Boltzmann sampling as a function of the J coupling energy scale programmed on the analog hardware (x axis), for the `Advantage2_system1.4` D-Wave quantum annealing processor. The bottom plot shows the value of the minimum error rate, TVD, found across all evaluated annealing times, and the top plot shows the corresponding β value at which the QPU samples a Boltzmann distribution at that given error rate. Each separate line denotes a different ANNNI model frustration parameter J_2.

of classical Boltzmann distributions. Nonetheless, this is an interesting property, in particular, because of the extremely fast simulation times, and therefore the overall low amount of QPU time used to obtain these approximate thermal distributions. One way of interpreting these very fast anneal quenches is that they are effectively quenching through the quantum magnetic phase diagram of the quantum ANNNI model [99], where the transverse field starts out dominating the system and then is very quickly quenched to zero transverse field.

TABLE II. Lowest error rate (TVD) D-Wave quantum processor results, for different ANNNI model frustration parameters J_2. All annealing times are in units of microseconds, and J denotes the overall hardware coupler scale factor.

Frustration parameter	`Advantage2_system1.4`	`Advantage_system4.1`
$J_2 = 0.01$	TVD $= 0.0138$, $\beta = 2.484$, AT $= 0.8$, $J = 0.95$	TVD $= 0.011$, $\beta = 1.451$, AT $= 0.1$, $J = 0.93$
$J_2 = 0.25$	TVD $= 0.0195$, $\beta = 2.613$, AT $= 0.7$, $J = 0.61$	TVD $= 0.0318$, $\beta = 1.953$, AT $= 2000$ $J = 0.51$
$J_2 = 0.49$	TVD $= 0.0381$, $\beta = 0.921$, AT $= 0.7$, $J = 0.1$	TVD $= 0.0261$, $\beta = 1.44$, AT $= 500$, $J = 0.26$
$J_2 = 0.5$	TVD $= 0.026$, $\beta = 1.43$, AT $= 0.8$, $J = 0.18$	TVD $= 0.0241$, $\beta = 1.521$, AT $= 2000$, $J = 0.27$
$J_2 = 0.51$	TVD $= 0.0236$, $\beta = 4.913$, AT $= 0.8$, $J = 0.25$	TVD $= 0.0212$, $\beta = 3.414$, AT $= 1400$, $J = 0.51$
$J_2 = 0.75$	TVD $= 0.0085$, $\beta = 3.257$, AT $= 1600$, $J = 0.56$	TVD $= 0.018$, $\beta = 2.579$, AT $= 1500$, $J = 0.83$
$J_2 = 1.0$	TVD $= 0.0003$, $\beta = 32.166$, AT $= 26$, $J = 0.87$	TVD $= 0.0067$, $\beta = 1.84$, AT $= 800$, $J = 0.36$

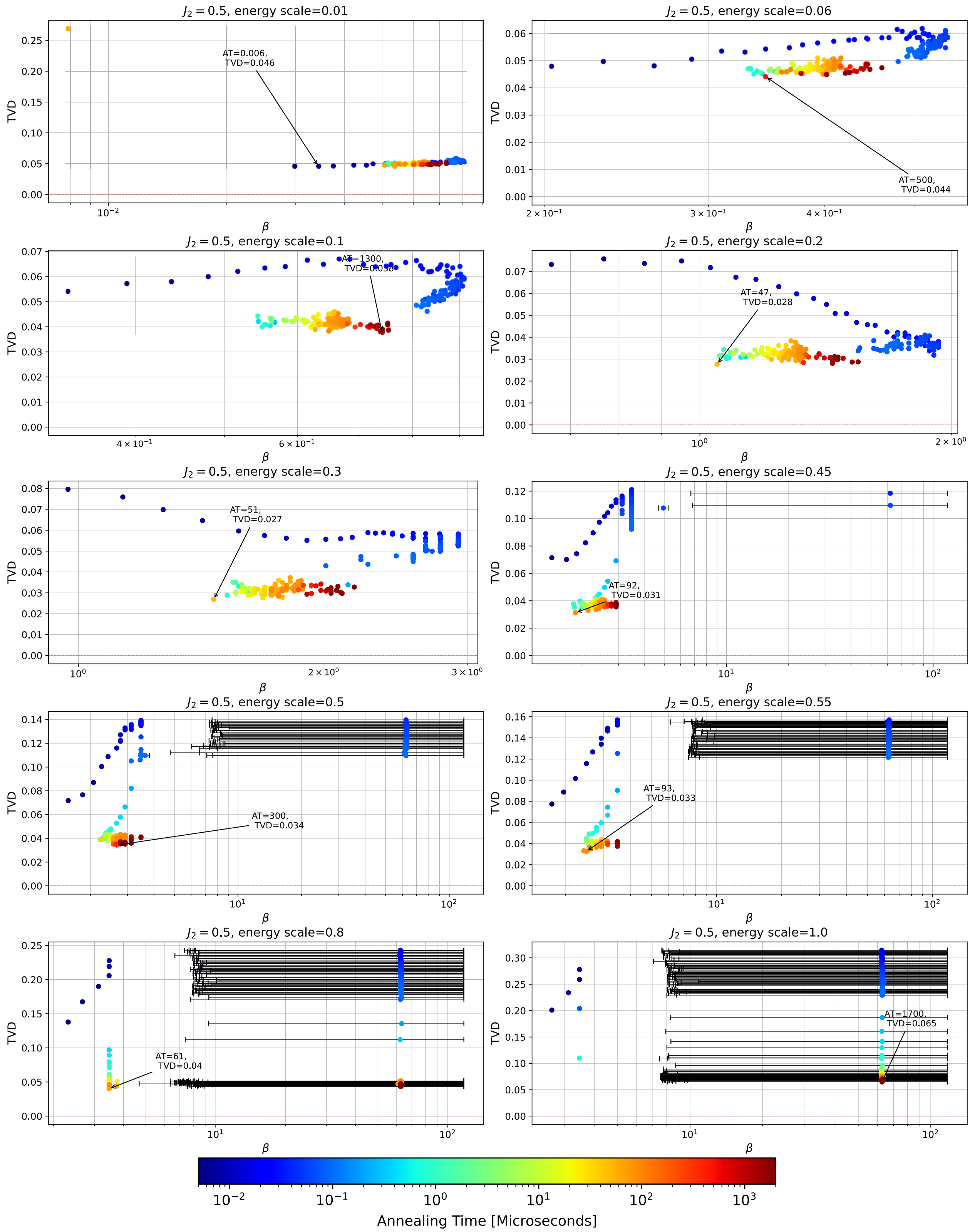

FIG. 4. Error rate (TVD) as a function of inverse temperature β, across the entire spectrum of evaluated annealing times (color coded by the log-scale heatmap below the subplots), for the ANNNI frustration parameter $J_2 = 0.5$ run on the `Advantage_system4.1` processor. Each subplot corresponds to a different analog hardware energy scale, denoted in the title of each subplot. Error bars are shown on data points where there were many best-fitted β values that spanned at least a range of 0.1. The annealing time that had the absolute lowest error rate within each subplot is annotated on the plot with the exact annealing time and the resulting TVD.

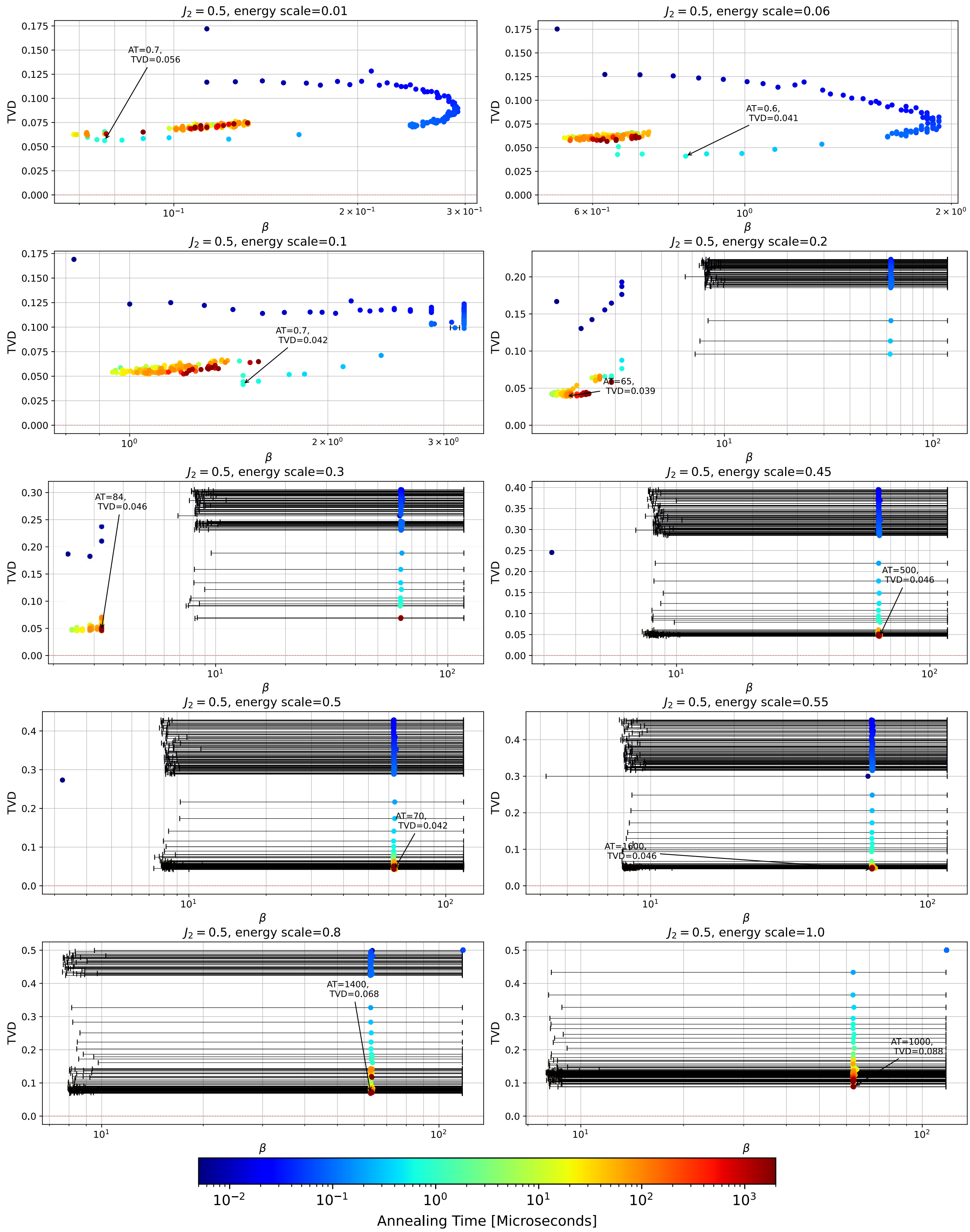

FIG. 5. Error rate (TVD) as a function of inverse temperature β, across the entire spectrum of evaluated annealing times (color coded by the log-scale heatmap below the subplots), for the ANNNI frustration parameter $J_2 = 0.5$ run on the `Advantage2_system1.4` processor. Each subplot corresponds to a different analog hardware energy scale, denoted in the title of each subplot. Error bars are shown on data points where there were many best-fitted β values that spanned at least a range of 0.1. The annealing time that had the absolute lowest error rate within each subplot is annotated on the plot with the exact annealing time and the resulting TVD.

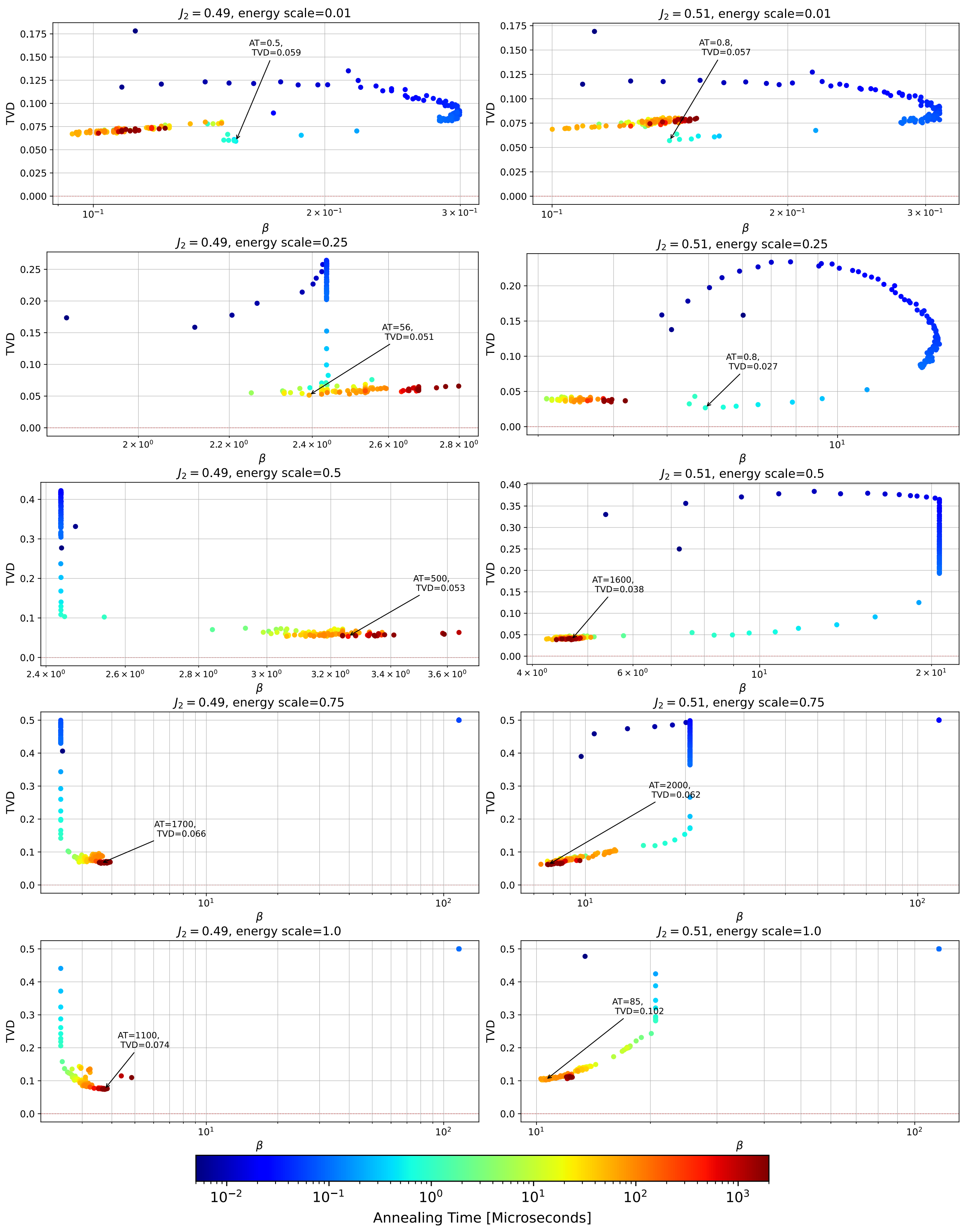

FIG. 6. `Advantage2_system1.4`, comparing results for the ANNNI frustration parameters $J = 0.49$ (left column) compared to $J = 0.51$ (right column) at different overall coupler energy scales (rows).

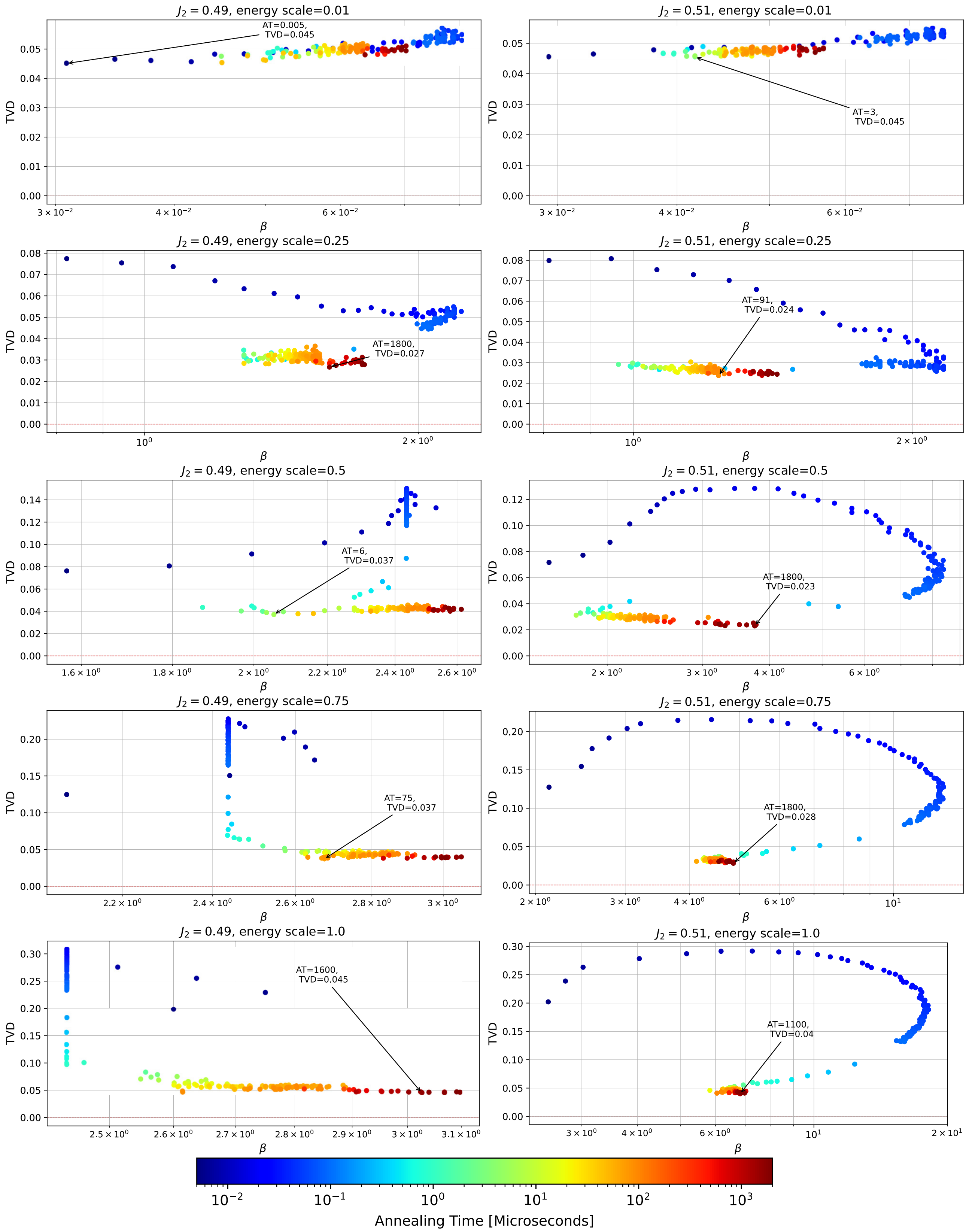

FIG. 7. `Advantage_system4.1`, comparing results for the ANNNI frustration parameters $J = 0.49$ (left column) compared to $J = 0.51$ (right column) at different overall coupler energy scales (rows).

IV. DISCUSSION AND CONCLUSION

This study has shown that analog quantum computers, specifically noisy superconducting qubit quantum annealers, are good Boltzmann samplers of highly frustrated Ising models such as the ANNNI model at various magnetic frustration parameters. Remarkably, this includes being able to sample at very low error rate (TVD 0.0003) the ANNNI model at $J_2 = 1$ at a low temperature ($\beta = 32.166$).

Interestingly, the sampling did become worse at and near the critical frustration point of $J_2 = 0.5$. This suggests that very high degeneracy and frustration do pose a problem for the analog hardware to accurately sample from an unbiased Boltzmann distribution. Moreover, the sampling characteristics are quite sensitive to where the ANNNI model is in its magnetic phase diagram with respect to the frustration parameter J_2; namely, clear differences are seen at, and on either side of, the critical frustration point $J_2 = 0.5$. This suggests that sampling on the D-Wave hardware, regardless of how good of a thermal sampler it is, could be a probe of critical frustration points in magnetic models. An interesting topic of future study is the role of degeneracy lifting in the transverse field-driven D-Wave QPU sampling of the ANNNI model. For example, at the critical frustration point if there is substantial degeneracy lifting of some of the ground-state configurations, that could explain why the sampling is worse at that point. Moreover, a lack of degeneracy lifting within the antiphase region ($J_2 = 1$) could explain why the noisy thermal sampling yields a very low error rate in that region of the ANNNI model. This is speculative; the role of degeneracy lifting was not quantified in the reported results.

The clearest open question is whether this Boltzmann sampling technique on D-Wave quantum annealers can be significantly scaled up in system size, and whether those simulations can compete with state-of-the-art classical heuristic methods, namely, the many Monte Carlo variants. The primary open question here is whether there are diagnostics that can be applied to the D-Wave QPU simulations that are proxies for the quality of the thermal sampling being performed. For sufficiently large system sizes, classical Monte Carlo methods may begin to struggle, and so an interesting open question is whether there are techniques that can be applied in order to validate equivalent D-Wave QPU sampling. There is no reason to expect that D-Wave quantum annealers will begin to fail at thermal sampling at larger system sizes; prior studies have demonstrated Gibbs sampling on reasonably large Ising models [30], and there is no indication of systematic errors that would hinder the D-Wave hardware. It would be very interesting to show that D-Wave analog quantum computers can outperform state-of-the-art classical methods for sufficiently large system sizes at the task of low-temperature sampling the Boltzmann distribution of a frustrated J_1-J_2 Ising model, in particular, at known frustration points in the model phase diagram. Related to this, it would be useful to validate whether the best-performing D-Wave analog hardware parameters, shown in Table II, are size independent. If this is the case, then that would show that D-Wave hardware is a very valuable Boltzmann sampler—being able to sample from the Boltzmann distribution of the frustrated ANNNI model at significantly larger system sizes.

ACKNOWLEDGMENTS

This work was supported by the U.S. Department of Energy through the Los Alamos National Laboratory. Los Alamos National Laboratory is operated by Triad National Security, LLC, for the National Nuclear Security Administration of the U.S. Department of Energy (Contract No. 89233218CNA000001). The research presented in this article was supported by the Laboratory Directed Research and Development program of Los Alamos National Laboratory under Project No. 20240032DR. This research used resources provided by the Los Alamos National Laboratory Institutional Computing Program. The author would also like to thank the New Mexico Consortium, under Subcontract No. C2778, the Quantum Cloud Access Project (QCAP), for providing quantum computing resources. LANL report LA-UR-25-30042.

DATA AVAILABILITY

There is no publicly available research data or software supporting this manuscript. Requests for further information or data should be sent to the authors.

APPENDIX A: D-WAVE QPU ANNEAL SCHEDULE ENERGY SCALES

Because all of the programmed units are in hardware-specific and normalized parameters, the physical units are not clear. Therefore, in Fig. 8 we show the full anneal schedules of the functions $A(s)$ and $B(s)$, which, for example, give the physical energy units for the J coupler energy scales.

APPENDIX B: D-WAVE HARDWARE GRAPH EMBEDDINGS

Figure 9 shows the exact $N = 12$ ANNNI model disjoint embeddings, with periodic boundaries, on the two D-Wave hardware graphs.

APPENDIX C: β VERSUS TVD EXAMPLE DATA FITTING

Figure 10 reports some example β versus TVD fitting curves. These illustrate the process of finding the overall lowest error (TVD) that a given quantum annealer sampling distribution has with respect to the ground truth of the full Boltzmann distribution. Importantly, in some cases,

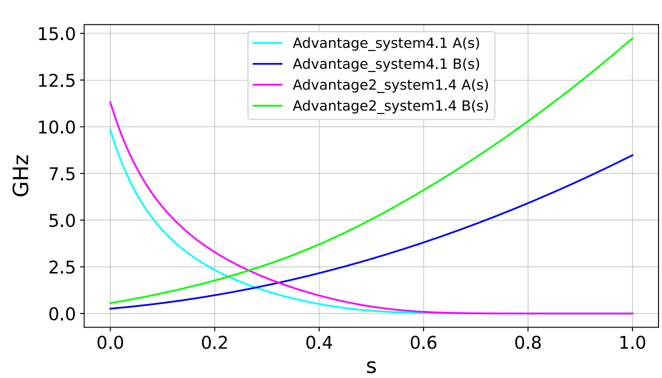

FIG. 8. D-Wave QPU hardware time-dependent Hamiltonian energy scale functions $A(s)$ and $B(s)$.

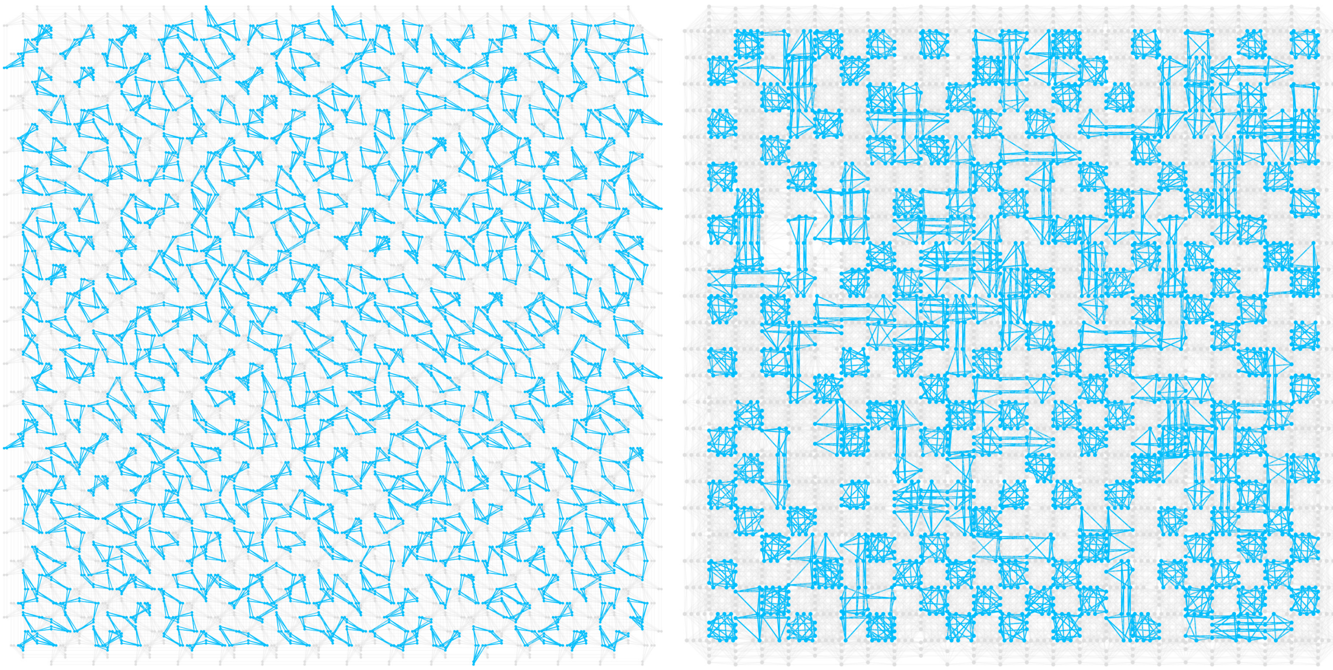

FIG. 9. Disjoint native (spin-to-qubit mappings) of multiple $N = 12$ ANNNI models onto the hardware graphs of `Advantage_system4.1` (left) and `Advantage2_system1.5` (right). Blue qubits (nodes) and blue couplers (edges) are used in the embeddings, and gray nodes/edges indicate unused hardware.

the lowest TVD β is uniquely determined; in other cases, it is not uniquely determined. So as to counteract potential numerical instability by reporting either the largest or the smallest β, in cases of a nonunique minimum error β, here we report the mean β. This process, for each physical analog set of parameters, involves searching over many orders of magnitude of β values and selecting the lowest found TVD.

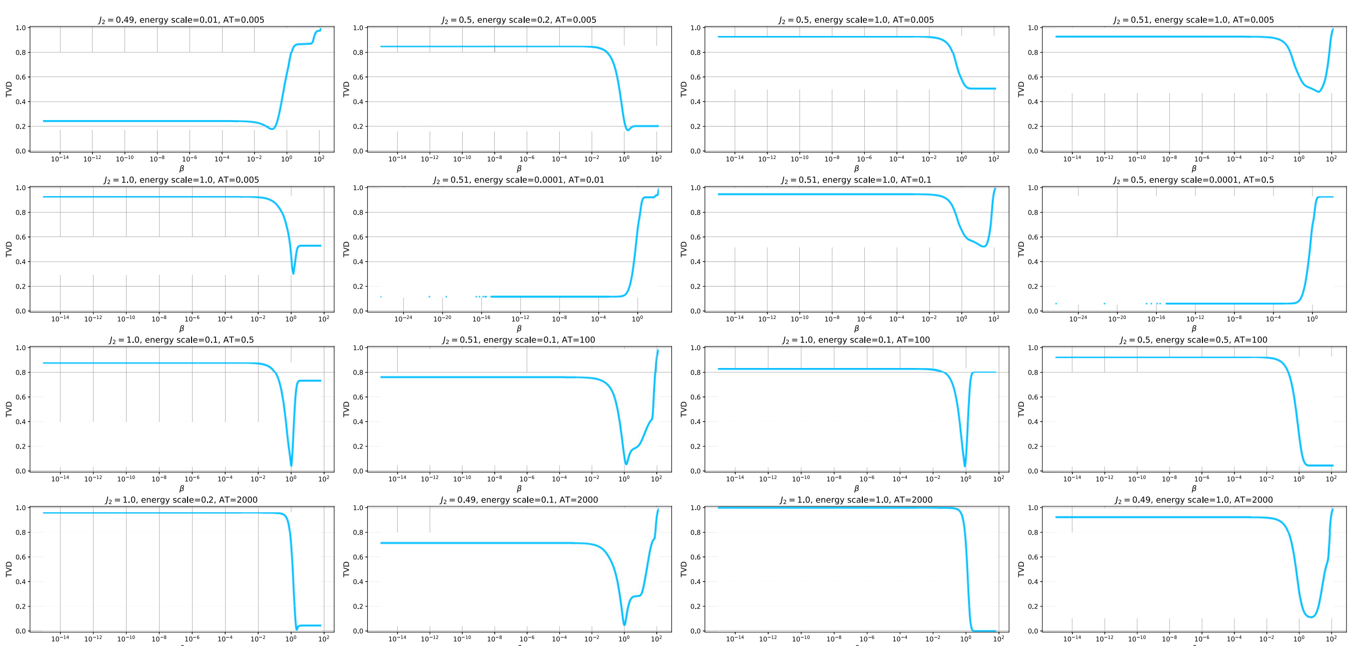

FIG. 10. Representative examples of the β fitting search landscape where the TVD is plotted as a function of a large search over many orders of magnitude of β values. Each plot corresponds to the measurements collected using a particular QPU analog hardware parameter set, which is specified in the title of each subplot (AT is an abbreviation of annealing time), and all data are from the `Advantage2_system1.4` processor. This shows that in some instances there is a clearly defined unique minimum, whereas in other instances there are many β values that result in the same error rate (a case where this occurs frequently is at higher-temperature sampling, such as when the coupler energy scale is set to near or effectively zero due to precision limits on the hardware).

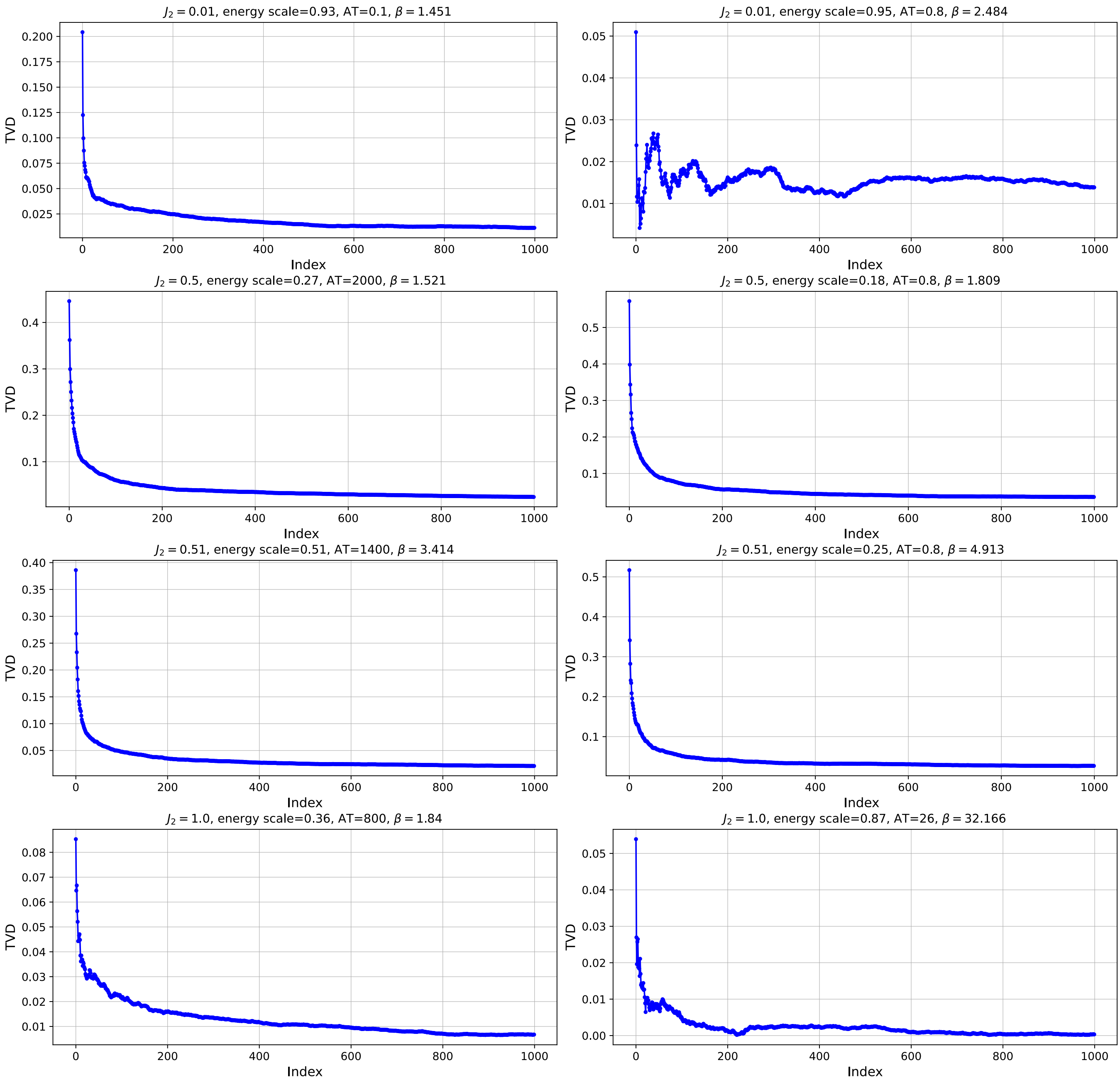

FIG. 11. Convergence analysis with respect to total sample count (x axis) for a representative set of the lowest error rate distributions. The x axis is an anneal index, where each anneal is comprised of many independent tiled copies of the Ising model. Data from the `Advantage_system4.1` processor (left) and the `Advantage2_system1.4` processor (right).

APPENDIX D: SUBSAMPLING BOOTSTRAP ERROR CONVERGENCE ANALYSIS

Figure 11 shows the subsampling analysis of some of the lowest error rate distributions. This shows that overall the error rates are reasonably stable once a sufficient number of samples are obtained.

APPENDIX E: ADDITIONAL ERROR VERSUS TEMPERATURE SAMPLING TRADE-OFF SCATTERPLOTS

Figure 12 shows complete error rate versus β distributions for the full range of annealing times, at the $J_2 = 1$ ANNNI frustration parameter. Similarly, Fig. 13 shows the same for

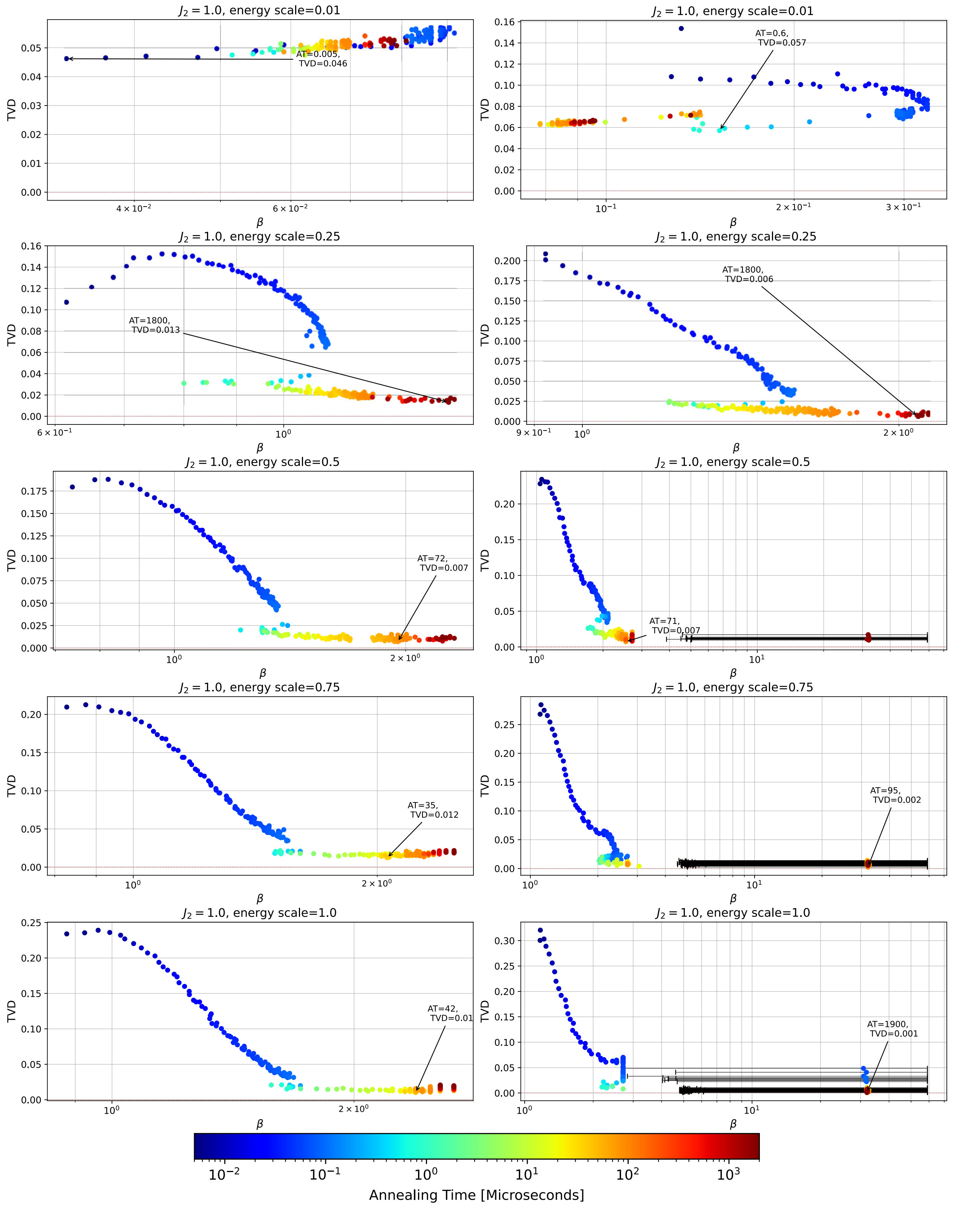

FIG. 12. $J_2 = 1$ ANNNI frustration parameter, run on `Advantage2_system1.4` (right column) and `Advantage_system4.1` (left column).

$J_2 = 0.75$, Fig. 14 shows the same for $J_2 = 0.25$, and Fig. 15 shows the same for $J_2 = 0.01$. Interestingly, similar to the $J_2 = 0.5$ results shown in the main text, Figs. 12 and 15 show us that $J_2 = 0.01$ and $J_2 = 1$ also result in some uncertainty in the sampled effective temperature, albeit only at some of the annealing times.

Figures 16 and 17 both show error rate as a function of inverse temperature β distributions when the overall J

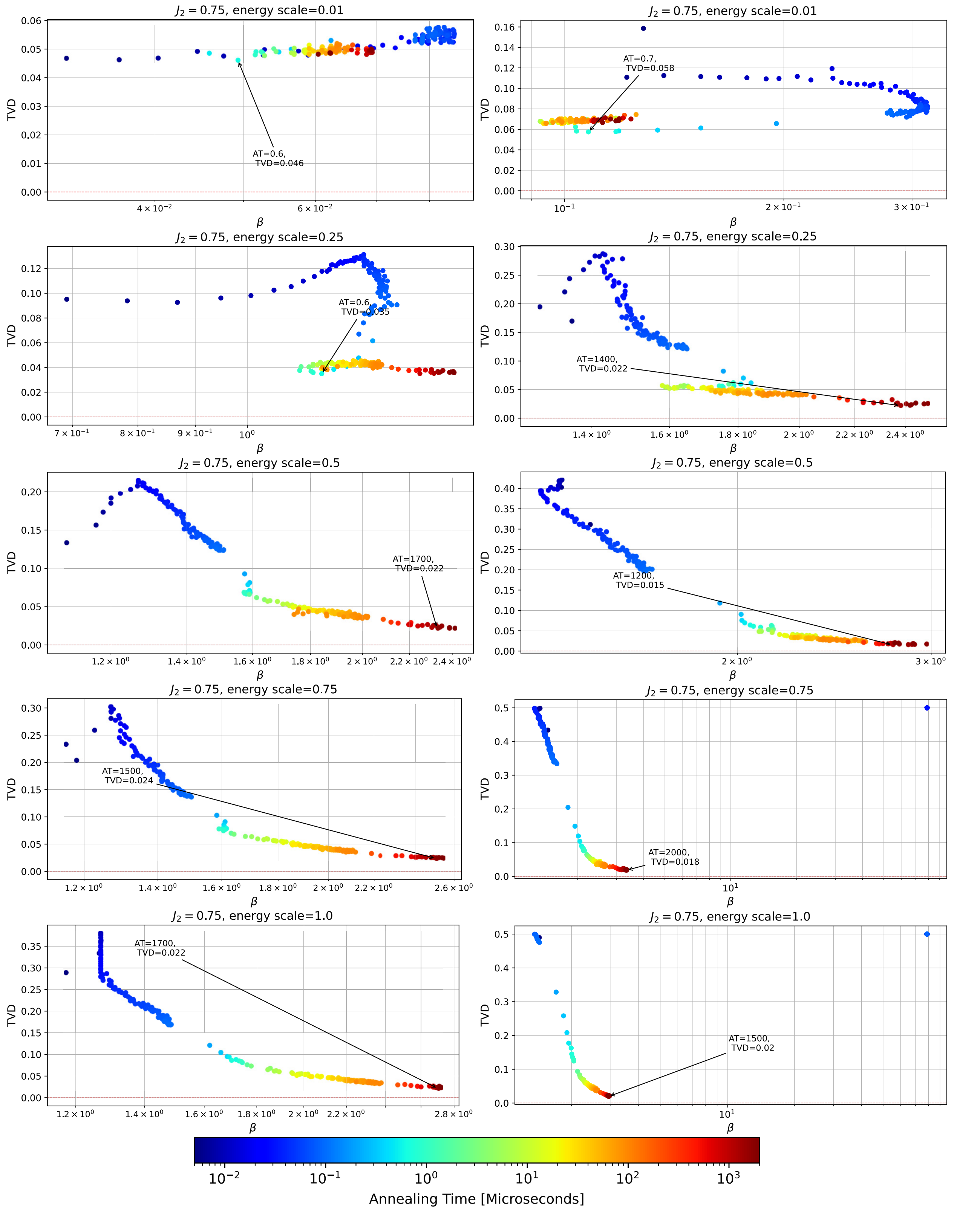

FIG. 13. $J_2 = 0.75$ ANNNI frustration parameter, run on `Advantage2_system1.4` (right column) and `Advantage_system4.1` (left column).

energy scale is very small—0.001. This means that the effective temperature of the sampling on the hardware is quite high. Importantly, this shows that this coupler energy scale is close to the overall analog precision limit on the hardware, and, in particular, when the frustration parameter J_2 is small in these plots, the effective antiferromagnetic couplers on the hardware are very likely effectively zero.

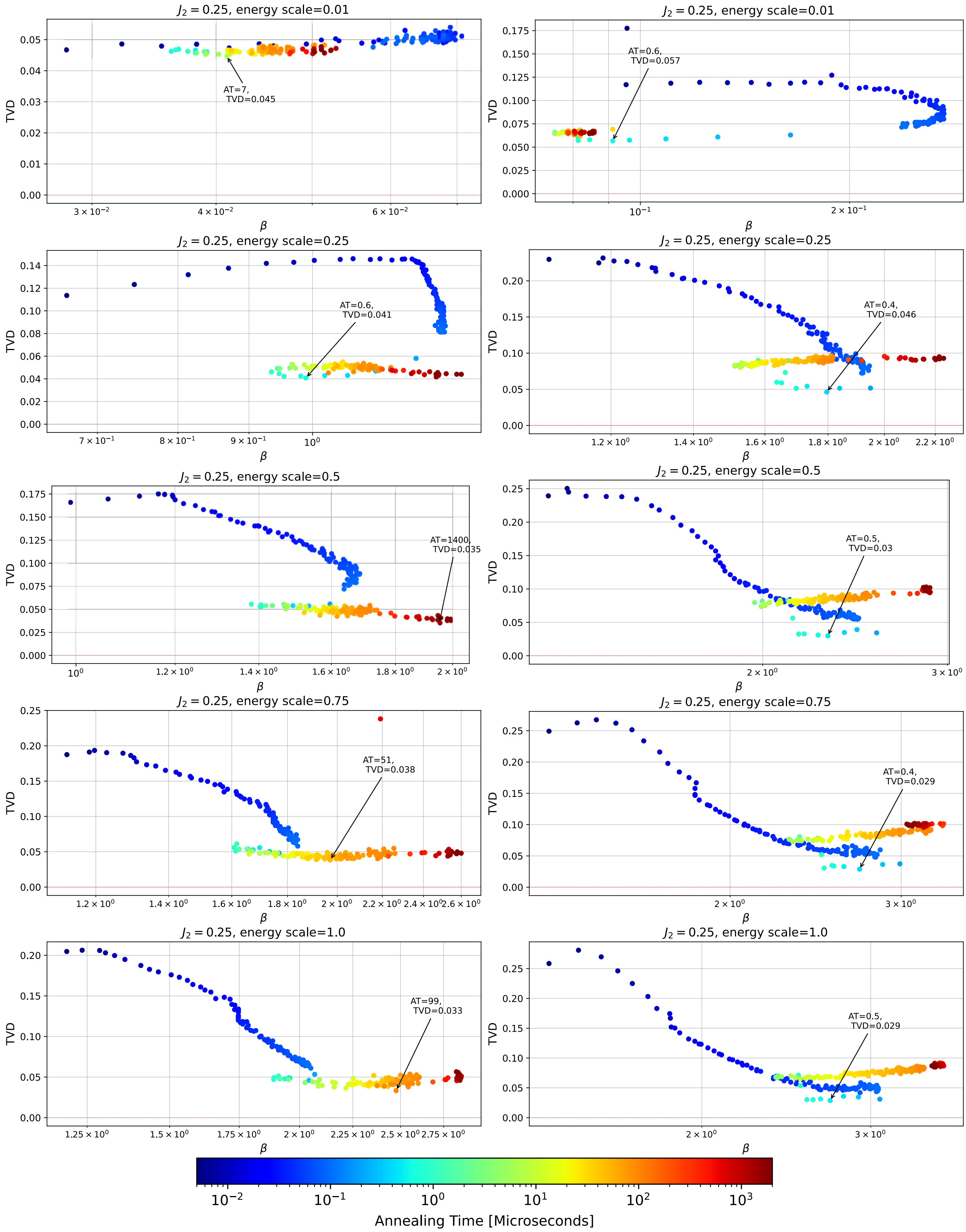

FIG. 14. $J_2 = 0.25$ ANNNI frustration parameter, run on `Advantage2_system1.4` (right column) and `Advantage_system4.1` (left column).

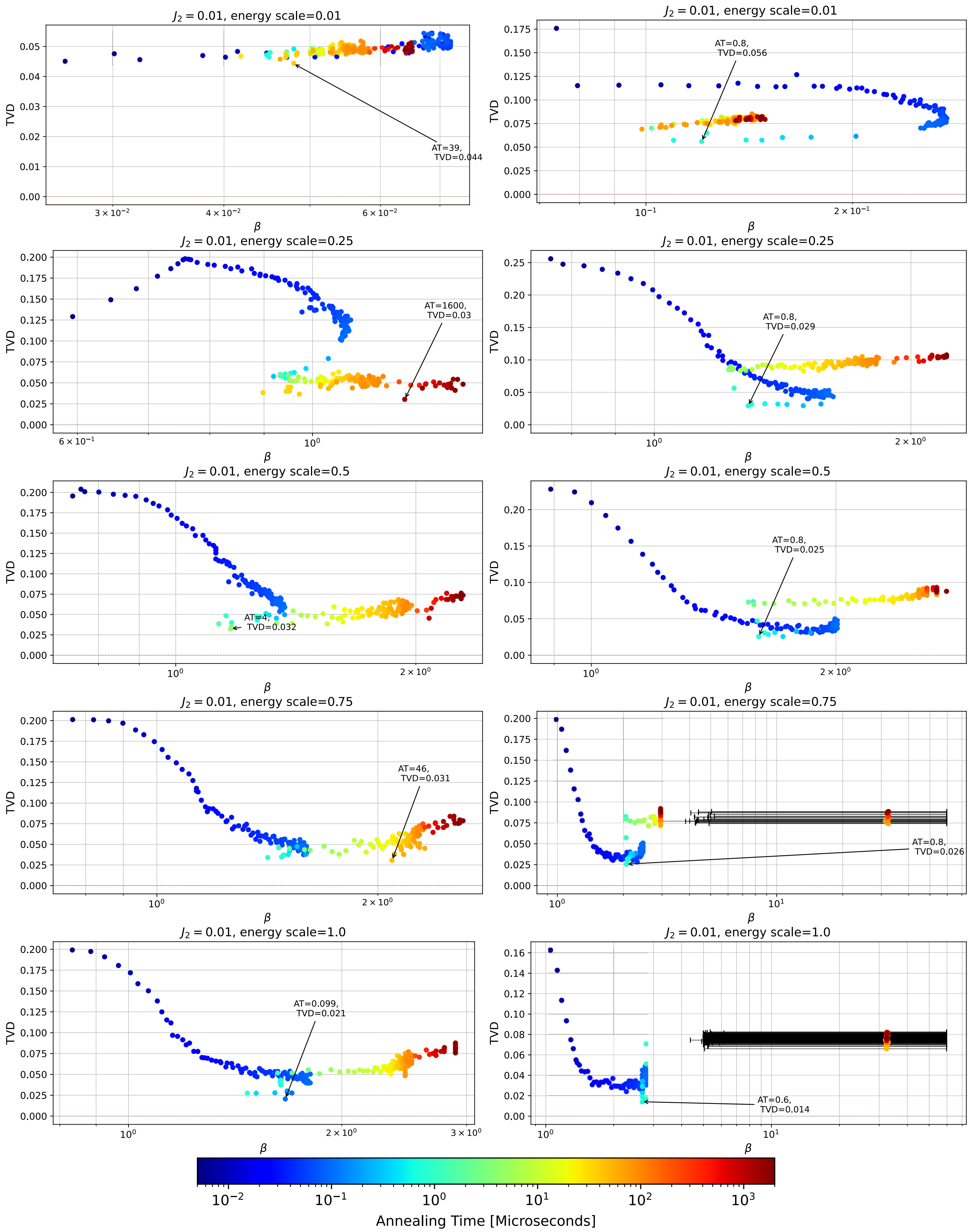

FIG. 15. $J_2 = 0.01$ ANNNI frustration parameter, run on `Advantage2_system1.4` (right column) and `Advantage_system4.1` (left column).

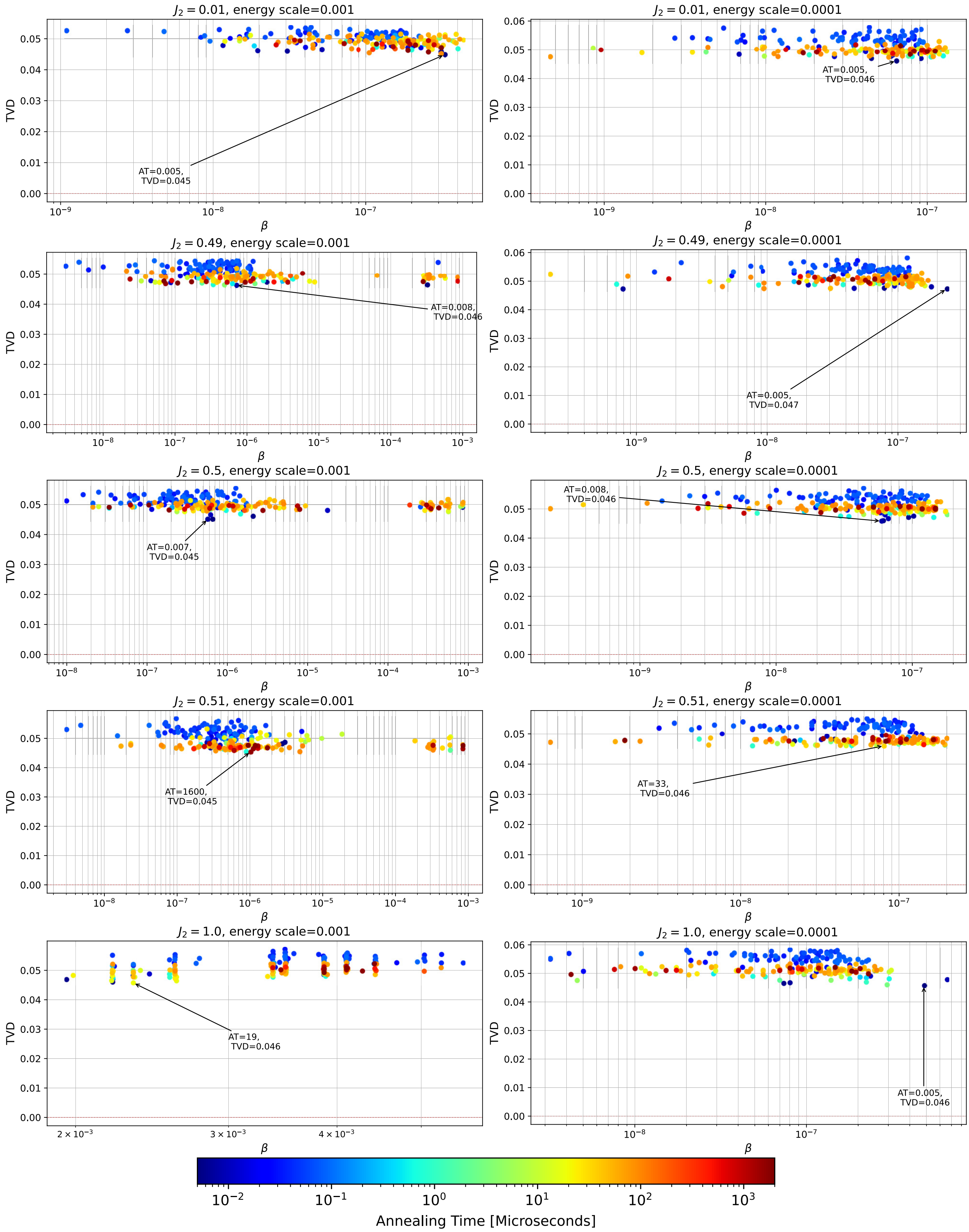

FIG. 16. Comparing small energy scales on the analog hardware, with an overall J coupler energy scale of 0.001 (left column) and 0.0001 (right column). Results from `Advantage_system4.1`.

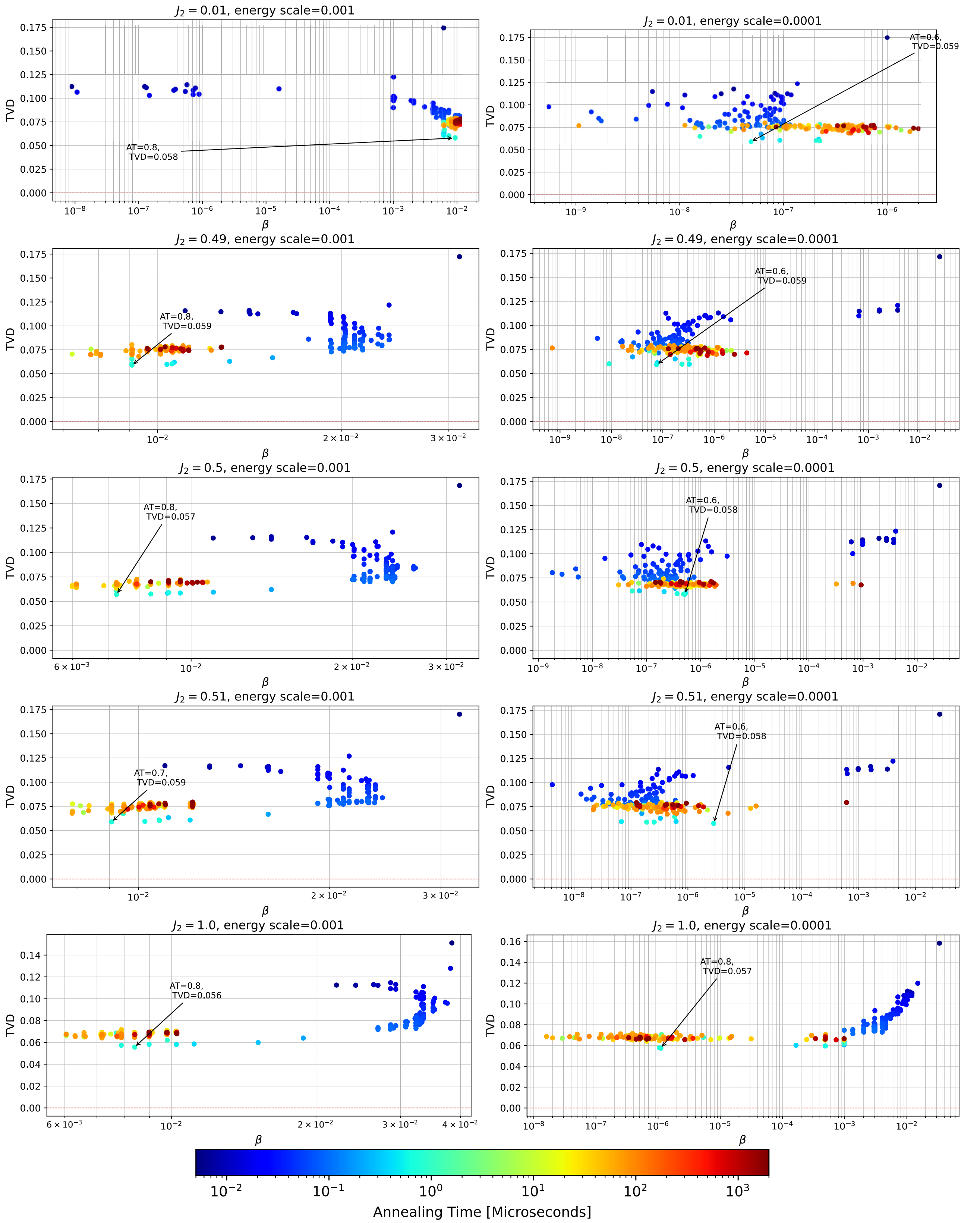

FIG. 17. Comparing small energy scales on the analog hardware, with an overall J scale of 0.001 (left column) and 0.0001 (right column). Results from `Advantage2_system1.4`.

[1] R. J. Elliott, Phenomenological discussion of magnetic ordering in the heavy rare-earth metals, Phys. Rev. **124**, 346 (1961).
[2] M. E. Fisher and W. Selke, Infinitely many commensurate phases in a simple Ising model, Phys. Rev. Lett. **44**, 1502 (1980).
[3] W. Selke, The ANNNI model—Theoretical analysis and experimental application, Phys. Rep. **170**, 213 (1988).
[4] M. E. Fisher and W. Selke, Low temperature analysis of the axial next-nearest neighbour Ising model near its multiphase point, Philos. Trans. R. Soc. A **302**, 1 (1981).
[5] F. Sciortino, S. Mossa, E. Zaccarelli, and P. Tartaglia, Equilibrium cluster phases and low-density arrested disordered states: The role of short-range attraction and long-range repulsion, Phys. Rev. Lett. **93**, 055701 (2004).
[6] H. Rieger and G. Uimin, The one-dimensional ANNNI model in a transverse field: Analytic and numerical study of effective Hamiltonians, Z. Phys. B **101**, 597 (1996).
[7] E. Rastelli, S. Regina, and A. Tassi, Specific heat and structure factor in the square ANNNI model by Monte Carlo simulation, Phys. Rev. B **81**, 094425 (2010).
[8] M. D. Grynberg and B. Tanatar, Square Ising model with second-neighbor interactions and the Ising chain in a transverse field, Phys. Rev. B **45**, 2876 (1992).
[9] A. Dutta, G. Aeppli, B. K. Chakrabarti, U. Divakaran, T. F. Rosenbaum, and D. Sen, Quantum phase transitions in transverse field spin models: From statistical physics to quantum information, arXiv:1012.0653.
[10] A. K. Chandra and S. Dasgupta, Floating phase in a 2D ANNNI model, J. Phys. A: Math. Theor. **40**, 6251 (2007).
[11] T. Kadowaki and H. Nishimori, Quantum annealing in the transverse Ising model, Phys. Rev. E **58**, 5355 (1998).
[12] G. E. Santoro and E. Tosatti, Optimization using quantum mechanics: Quantum annealing through adiabatic evolution, J. Phys. A: Math. Gen. **39**, R393 (2006).
[13] G. E. Santoro, R. Martoňák, E. Tosatti, and R. Car, Theory of quantum annealing of an Ising spin glass, Science **295**, 2427 (2002).
[14] S. Morita and H. Nishimori, Mathematical foundation of quantum annealing, J. Math. Phys. **49**, 125210 (2008).
[15] E. Farhi, J. Goldstone, S. Gutmann, and M. Sipser, Quantum computation by adiabatic evolution, arXiv:quant-ph/0001106.
[16] R. Harris, Y. Sato, A. J. Berkley, M. Reis, F. Altomare, M. Amin, K. Boothby, P. Bunyk, C. Deng, C. Enderud, *et al.*, Phase transitions in a programmable quantum spin glass simulator, Science **361**, 162 (2018).
[17] A. D. King, A. Nocera, M. M. Rams, J. Dziarmaga, R. Wiersema, W. Bernoudy, J. Raymond, N. Kaushal, N. Heinsdorf, R. Harris, *et al.*, Beyond-classical computation in quantum simulation, Science **388**, 199 (2025).
[18] A. D. King, C. D. Batista, J. Raymond, T. Lanting, I. Ozfidan, G. Poulin-Lamarre, H. Zhang, and M. H. Amin, Quantum annealing simulation of out-of-equilibrium magnetization in a spin-chain compound, PRX Quantum **2**, 030317 (2021).
[19] A. D. King, C. Nisoli, E. D. Dahl, G. Poulin-Lamarre, and A. Lopez-Bezanilla, Qubit spin ice, Science **373**, 576 (2021).
[20] P. Kairys, A. D. King, I. Ozfidan, K. Boothby, J. Raymond, A. Banerjee, and T. S. Humble, Simulating the Shastry-Sutherland Ising model using quantum annealing, PRX Quantum **1**, 020320 (2020).
[21] E. Pelofske, A. Bärtschi, and S. Eidenbenz, Simulating heavy-hex transverse field Ising model magnetization dynamics using programmable quantum annealers, arXiv:2311.01657.
[22] P. Narasimhan, S. Humeniuk, A. Roy, and V. Drouin-Touchette, Simulating the transverse-field Ising model on the kagome lattice using a programmable quantum annealer, Phys. Rev. B **110**, 054432 (2024).
[23] J. Marshall, D. Venturelli, I. Hen, and E. G. Rieffel, Power of pausing: Advancing understanding of thermalization in experimental quantum annealers, Phys. Rev. Appl. **11**, 044083 (2019).
[24] Z. G. Izquierdo, I. Hen, and T. Albash, Testing a quantum annealer as a quantum thermal sampler, ACM Trans. Quantum Comput. **2**, 1 (2021).
[25] J. Marshall, E. G. Rieffel, and I. Hen, Thermalization, freeze-out, and noise: Deciphering experimental quantum annealers, Phys. Rev. Appl. **8**, 064025 (2017).
[26] J. Nelson, M. Vuffray, A. Y. Lokhov, and C. Coffrin, Single-qubit fidelity assessment of quantum annealing hardware, IEEE Trans. Quantum Eng. **2**, 1 (2021).
[27] M. Vuffray, C. Coffrin, Y. A. Kharkov, and A. Y. Lokhov, Programmable quantum annealers as noisy Gibbs samplers, PRX Quantum **3**, 020317 (2022).
[28] J. Nelson, M. Vuffray, A. Y. Lokhov, T. Albash, and C. Coffrin, High-quality thermal Gibbs sampling with quantum annealing hardware, Phys. Rev. Appl. **17**, 044046 (2022).
[29] L. Buffoni and M. Campisi, Thermodynamics of a quantum annealer, Quantum Sci. Technol. **5**, 035013 (2020).
[30] P. Sathe, A. D. King, S. M. Mniszewski, C. Coffrin, C. Nisoli, and F. Caravelli, Classical criticality via quantum annealing, Nat. Commun. **17**, 856 (2025).
[31] J. Raymond, S. Yarkoni, and E. Andriyash, Global warming: Temperature estimation in annealers, Front. ICT **3**, 23 (2016).
[32] R. Sandt and R. Spatschek, Efficient low temperature Monte Carlo sampling using quantum annealing, Sci. Rep. **13**, 6754 (2023).
[33] R. Shibukawa, R. Tamura, and K. Tsuda, Boltzmann sampling with quantum annealers via fast Stein correction, Phys. Rev. Res. **6**, 043050 (2024).
[34] N. Chancellor, S. Szoke, W. Vinci, G. Aeppli, and P. A. Warburton, Maximum-entropy inference with a programmable annealer, Sci. Rep. **6**, 22318 (2016).
[35] X. Tan, J. Li, and P. Stoica, Efficient sparse Bayesian learning via Gibbs sampling, in *2010 IEEE International Conference on Acoustics, Speech and Signal Processing* (IEEE, New York, 2010), pp. 3634–3637.
[36] N. Metropolis, A. W. Rosenbluth, M. N. Rosenbluth, A. H. Teller, and E. Teller, Equation of state calculations by fast computing machines, J. Chem. Phys. **21**, 1087 (1953).
[37] S. Andrews, H. De Sterck, S. Inglis, and R. G. Melko, Monte Carlo study of degenerate ground states and residual entropy in a frustrated honeycomb lattice Ising model, Phys. Rev. E **79**, 041127 (2009).
[38] N. Huang, W. Perkins, and A. Potechin, Hardness of sampling for the anti-ferromagnetic Ising model on random graphs, arXiv:2409.03974.
[39] L. Spiridon and D. D. Minh, Hamiltonian Monte Carlo with constrained molecular dynamics as Gibbs sampling, J. Chem. Theory Comput. **13**, 4649 (2017).

[40] O. Bodini and Y. Ponty, Multi-dimensional Boltzmann sampling of languages, Discrete Math. Theor. Comput. Sci. (2010).
[41] F. Noé, S. Olsson, J. Köhler, and H. Wu, Boltzmann generators: Sampling equilibrium states of many-body systems with deep learning, Science **365**, eaaw1147 (2019).
[42] H. Goto, Z. Lin, and Y. Nakamura, Boltzmann sampling from the Ising model using quantum heating of coupled nonlinear oscillators, Sci. Rep. **8**, 7154 (2018).
[43] G. Margiani, O. Ameye, O. Zilberberg, and A. Eichler, Three strongly coupled Kerr parametric oscillators forming a Boltzmann machine, Phys. Rev. Lett. **135**, 097201 (2025).
[44] G. Margiani, J. del Pino, T. L. Heugel, N. E. Bousse, S. Guerrero, T. W. Kenny, O. Zilberberg, D. Sabonis, and A. Eichler, Deterministic and stochastic sampling of two coupled Kerr parametric oscillators, Phys. Rev. Res. **5**, L012029 (2023).
[45] H. Hasegawa and N. Shibata, Residual errors after quantum annealing in the axial next nearest neighbor Ising model: Impact of critical points and modulated correlation, J. Phys. Soc. Jpn. **94**, 094004 (2025).
[46] G. E. L. Pexe, L. A. M. Rattighieri, A. L. Malvezzi, and F. F. Fanchini, Using a feedback-based quantum algorithm to analyze the critical properties of the ANNNI model without classical optimization, Phys. Rev. B **110**, 224422 (2024).
[47] M. Cea, M. Grossi, S. Monaco, E. Rico, L. Tagliacozzo, and S. Vallecorsa, Exploring the phase diagram of the quantum one-dimensional ANNNI model, arXiv:2402.11022.
[48] C. Marin, A. Fontana, V. Bellani, F. Pederiva, A. Quaranta, F. Rossella, A. Salamon, and G. Salina, Modeling a frustrated Ising square lattice with the D-Wave quantum annealer, arXiv:2409.11259.
[49] M. W. Johnson, M. H. Amin, S. Gildert, T. Lanting, F. Hamze, N. Dickson, R. Harris, A. J. Berkley, J. Johansson, P. Bunyk, *et al.*, Quantum annealing with manufactured spins, Nature (London) **473**, 194 (2011).
[50] P. I. Bunyk, E. M. Hoskinson, M. W. Johnson, E. Tolkacheva, F. Altomare, A. J. Berkley, R. Harris, J. P. Hilton, T. Lanting, A. J. Przybysz, and J. Whittaker, Architectural considerations in the design of a superconducting quantum annealing processor, IEEE Trans. Appl. Supercond. **24**, 1 (2014).
[51] N. G. Dickson, M. W. Johnson, M. Amin, R. Harris, F. Altomare, A. J. Berkley, P. Bunyk, J. Cai, E. Chapple, P. Chavez, *et al.*, Thermally assisted quantum annealing of a 16-qubit problem, Nat. Commun. **4**, 1903 (2013).
[52] R. Harris, M. W. Johnson, T. Lanting, A. J. Berkley, J. Johansson, P. Bunyk, E. Tolkacheva, E. Ladizinsky, N. Ladizinsky, T. Oh, *et al.*, Experimental investigation of an eight-qubit unit cell in a superconducting optimization processor, Phys. Rev. B **82**, 024511 (2010).
[53] M. W. Johnson, P. Bunyk, F. Maibaum, E. Tolkacheva, A. J. Berkley, E. M. Chapple, R. Harris, J. Johansson, T. Lanting, I. Perminov, E. Ladizinsky, T. Oh, and G. Rose, A scalable control system for a superconducting adiabatic quantum optimization processor, Supercond. Sci. Technol. **23**, 065004 (2010).
[54] Y. Matsuda, H. Nishimori, and H. G. Katzgraber, Quantum annealing for problems with ground-state degeneracy, in *Journal of Physics: Conference Series* (IOP Publishing, 2009), Vol. 143, p. 012003.
[55] E. Pelofske, J. Golden, A. Bärtschi, D. O'Malley, and S. Eidenbenz, Sampling on NISQ Devices "Who's the Fairest One of All?", in *2021 IEEE International Conference on Quantum Computing and Engineering (QCE)* (IEEE, New York, 2021), pp. 207–217.
[56] M. S. Könz, G. Mazzola, A. J. Ochoa, H. G. Katzgraber, and M. Troyer, Uncertain fate of fair sampling in quantum annealing, Phys. Rev. A **100**, 030303 (2019).
[57] S. Mandrà, Z. Zhu, and H. G. Katzgraber, Exponentially biased ground-state sampling of quantum annealing machines with transverse-field driving Hamiltonians, Phys. Rev. Lett. **118**, 070502 (2017).
[58] Z. Zhu, A. J. Ochoa, and H. G. Katzgraber, Fair sampling of ground-state configurations of binary optimization problems, Phys. Rev. E **99**, 063314 (2019).
[59] J. Job and D. Lidar, Test-driving 1000 qubits, Quantum Sci. Technol. **3**, 030501 (2018).
[60] T. Albash, W. Vinci, A. Mishra, P. A. Warburton, and D. A. Lidar, Consistency tests of classical and quantum models for a quantum annealer, Phys. Rev. A **91**, 042314 (2015).
[61] T. Albash and D. A. Lidar, Decoherence in adiabatic quantum computation, Phys. Rev. A **91**, 062320 (2015).
[62] S. Boixo, T. Albash, F. M. Spedalieri, N. Chancellor, and D. A. Lidar, Experimental signature of programmable quantum annealing, Nat. Commun. **4**, 2067 (2013).
[63] S. Redner, One-dimensional Ising chain with competing interactions: Exact results and connection with other statistical models, J. Stat. Phys. **25**, 15 (1981).
[64] Y. Hu and P. Charbonneau, Resolving the two-dimensional axial next-nearest-neighbor Ising model using transfer matrices, Phys. Rev. B **103**, 094441 (2021).
[65] J. Stephenson, Ising model with antiferromagnetic next-nearest-neighbor coupling: Spin correlations and disorder points, Phys. Rev. B **1**, 4405 (1970).
[66] Y. Hu and P. Charbonneau, Numerical transfer matrix study of frustrated next-nearest-neighbor Ising models on square lattices, Phys. Rev. B **104**, 144429 (2021).
[67] T. Shirakura, F. Matsubara, and N. Suzuki, Kosterlitz-Thouless phase transition of the axial next-nearest-neighbor Ising model in two dimensions, Phys. Rev. B **90**, 144410 (2014).
[68] A. Dhar, B. S. Shastry, and C. Dasgupta, Equilibrium and dynamical properties of the axial next-nearest-neighbor Ising chain at the multiphase point, Phys. Rev. E **62**, 1592 (2000).
[69] J. M. Yeomans, Splitting the multiphase point, arXiv:cond-mat/9506129.
[70] G. Torre, A. G. Catalano, S. B. Kožić, F. Franchini, and S. M. Giampaolo, Interplay between local and non-local frustration in the 1D ANNNI chain: I. The even case, J. Stat. Mech. (2025) 053101.
[71] C. McCreesh, P. Prosser, and J. Trimble, in *International Conference on Graph Transformation* (Springer, Cham, 2020), pp. 316–324.
[72] K. Chern, K. Boothby, J. Raymond, P. Farré, and A. D. King, Tutorial: Calibration refinement in quantum annealing, Front. Comput. Sci. **5**, 1238988 (2023).
[73] J. Cai, W. G. Macready, and A. Roy, A practical heuristic for finding graph minors, arXiv:1406.2741.

[74] E. Pelofske, G. Hahn, and H. N. Djidjev, Parallel quantum annealing, Sci. Rep. **12**, 4499 (2022).

[75] E. Pelofske, G. Hahn, D. O'Malley, H. N. Djidjev, and B. S. Alexandrov, Quantum annealing algorithms for Boolean tensor networks, Sci. Rep. **12**, 8539 (2022).

[76] N. Dattani, S. Szalay, and N. Chancellor, Pegasus: The second connectivity graph for large-scale quantum annealing hardware, arXiv:1901.07636.

[77] K. Boothby, P. Bunyk, J. Raymond, and A. Roy, Next-generation topology of D-Wave quantum processors, arXiv:2003.00133.

[78] K. Boothby, A. D. King, and J. Raymond, Zephyr topology of D-Wave quantum processors (2021), https://www.dwavesys.com/media/2uznec4s/14-1056a-a_zephyr_topology_of_dwave_quantum_processors.pdf.

[79] J. Marshall, A. Di Gioacchino, and E. G. Rieffel, Perils of embedding for sampling problems, Phys. Rev. Res. **2**, 023020 (2020).

[80] T. W. Kibble, Topology of cosmic domains and strings, J. Phys. A: Math. Gen. **9**, 1387 (1976).

[81] W. H. Zurek, Cosmological experiments in superfluid helium? Nature (London) **317**, 505 (1985).

[82] However, these very fast anneals are really quenches given the timescales involved.

[83] Y. Bando, Y. Susa, H. Oshiyama, N. Shibata, M. Ohzeki, F. J. Gómez-Ruiz, D. A. Lidar, S. Suzuki, A. Del Campo, and H. Nishimori, Probing the universality of topological defect formation in a quantum annealer: Kibble-Zurek mechanism and beyond, Phys. Rev. Res. **2**, 033369 (2020).

[84] A. D. King, J. Raymond, T. Lanting, R. Harris, A. Zucca, F. Altomare, A. J. Berkley, K. Boothby, S. Ejtemaee, C. Enderud, *et al.*, Quantum critical dynamics in a 5,000-qubit programmable spin glass, Nature (London) **617**, 61 (2023).

[85] A. D. King, S. Suzuki, J. Raymond, A. Zucca, T. Lanting, F. Altomare, A. J. Berkley, S. Ejtemaee, E. Hoskinson, S. Huang, *et al.*, Coherent quantum annealing in a programmable 2,000 qubit Ising chain, Nat. Phys. **18**, 1324 (2022).

[86] M. H. Amin, Searching for quantum speedup in quasistatic quantum annealers, Phys. Rev. A **92**, 052323 (2015).

[87] E. Pelofske, G. Hahn, and H. N. Djidjev, Noise dynamics of quantum annealers: Estimating the effective noise using idle qubits, Quantum Sci. Technol. **8**, 035005 (2023).

[88] Z. Morrell, M. Vuffray, A. Y. Lokhov, A. Bärtschi, T. Albash, and C. Coffrin, Signatures of open and noisy quantum systems in single-qubit quantum annealing, Phys. Rev. Appl. **19**, 034053 (2023).

[89] T. Zaborniak and R. de Sousa, Benchmarking Hamiltonian noise in the D-Wave quantum annealer, IEEE Trans. Quantum Eng. **2**, 1 (2021).

[90] C. Tüysüz, A. Jayakumar, C. Coffrin, M. Vuffray, and A. Y. Lokhov, Learning response functions of analog quantum computers: Analysis of neutral-atom and superconducting platforms, arXiv:2503.12520.

[91] T. Lanting, M. H. Amin, C. Baron, M. Babcock, J. Boschee, S. Boixo, V. N. Smelyanskiy, M. Foygel, and A. G. Petukhov, Probing environmental spin polarization with superconducting flux qubits, arXiv:2003.14244.

[92] P. Virtanen, R. Gommers, T. E. Oliphant, M. Haberland, T. Reddy, D. Cournapeau, E. Burovski, P. Peterson, W. Weckesser, J. Bright, *et al.*, SciPy 1.0: Fundamental algorithms for scientific computing in Python, Nat. Methods **17**, 261 (2020).

[93] F. Gao and L. Han, Implementing the Nelder-Mead simplex algorithm with adaptive parameters, Comput. Optim. Appl. **51**, 259 (2012).

[94] J. Nocedal and S. J. Wright, *Numerical Optimization* (Springer, Cham, 2006).

[95] A. R. Conn, N. I. Gould, and P. L. Toint, *Trust Region Methods* (SIAM, 2000).

[96] S. K. Lam, A. Pitrou, and S. Seibert, in *Proceedings of the Second Workshop on the LLVM Compiler Infrastructure in HPC*, LLVM '15 (Association for Computing Machinery, New York, 2015).

[97] C. R. Harris, K. J. Millman, S. J. van der Walt, R. Gommers, P. Virtanen, D. Cournapeau, E. Wieser, J. Taylor, S. Berg, N. J. Smith, *et al.*, Array programming with NumPy, Nature (London) **585**, 357 (2020).

[98] S. Suzuki, J.-I. Inoue, and B. K. Chakrabarti, *Quantum Ising Phases and Transitions in Transverse Ising Models* (Springer, Cham, 2012), Vol. 862.

[99] Perhaps analogous to similar types of quenches performed in Ref. [100], the difference being that in that study the quench was performed across frustration parameters, such as from the ferromagnetic phase into the antiphase.

[100] A. Haldar, K. Mallayya, M. Heyl, F. Pollmann, M. Rigol, and A. Das, Signatures of quantum phase transitions after quenches in quantum chaotic one-dimensional systems, Phys. Rev. X **11**, 031062 (2021).